AD A114189

4

Solid State Research

1981

Lincoln Laboratory

MASSACHUSETTS INSTITUTE OF TECHNOLOGY

LEXINGTON, MASSACHUSETTS

DTIC FILE COPY

DTIC
ELECTE
MAY 5 1982
S D
A

82 05 05 001

This technical report has been reviewed and is approved for publication.

FOR THE COMMANDER

Raymond L. Loiselle

Raymond L. Loiselle, Lt.Col., USAF
Chief, ESD Lincoln Laboratory Project Office

MASSACHUSETTS INSTITUTE OF TECHNOLOGY
LINCOLN LABORATORY

SOLID STATE RESEARCH

QUARTERLY TECHNICAL SUMMARY REPORT

1 AUGUST — 31 OCTOBER 1981

ISSUED 23 FEBRUARY 1982

LEXINGTON   MASSACHUSETTS

ABSTRACT

This report covers in detail the solid state research work of the Solid State
Division at Lincoln Laboratory for the period 1 August through 31 October 1981.
The topics covered are Solid State Device Research, Quantum Electronics,
Materials Research, Microelec.ronics, and Analog Device Technology. Funding
is primarily provided by the Air Force, with additional support provided by the
Army, DARPA, Navy, NASA, and DOE.

CONTENTS

INTRODUCTION

I. SOLID STATE DEVICE RESEARCH

The series combination of a semiconductor-diode gain element and an optical fiber has been operated inside an external cavity with an output at a single wavelength and a linewidth which was less than the measurement limit of 1.7×10^{-5} nm. The work is aimed toward demonstrating the feasibility of coupling semiconductor-diode lasers in parallel by using optical fibers and thus verifying the concept of a semiconductor laser system with average power up to the order of kilowatts.

InP optoelectronic switches have been fabricated which have fast response times (<100 ps) and high electron mobility ($\sim$1000 cm^2/V-s) following proton bombardment and anneal. These devices are well suited for high-speed sampling and mixing applications, especially those which require the absence of a DC offset and/or a high degree of isolation between the local oscillator and output. Other applications, such as optical detection, could make use of the high speed of these devices.

Hole diffusion lengths in n-InP of 12 μm have been determined by measuring the increase in collection efficiency of an InP avalanche photodiode as a function of reverse bias. This diffusion length is nearly an order of magnitude greater than the previously reported values measured by surface photovoltage and electron-beam-induced-current (EBIC) techniques.

A 4-bit, 275-MS/s guided-wave electrooptic analog-to-digital converter has been demonstrated. The device consists of a mode-locked Nd:YAG laser, an array of Ti-diffused LiNbO$_3$ interferometric modulators, a Ge avalanche photodiode, and a special high-speed Si integrated circuit.

Planar Hg-diffused Hg$_{0.824}$Cd$_{0.176}$Te photodiodes have been fabricated and operated at 20 K with cutoff wavelengths of over 30 μm and response times of less than 0.6 ns at a wavelength of 20 μm. These devices are being developed for use as wide-bandwidth heterodyne receivers at 28 μm for astrophysical applications.

II. QUANTUM ELECTRONICS

Remote sensing measurements of the toxic compounds hydrazine, unsymmetrical dimethylhydrazine (UDMH), and monomethylhydrazine (MMH) have been carried out using LIDAR returns from a diffusely reflecting target located 2.7 km from the laboratory. The results indicate that atmospheric fluctuation is the dominant factor limiting the detection sensitivity of these compounds over ranges between 0.5 and 5 km.

Raman measurements of the stress in silicon-on-sapphire device structures have been carried out with an approximately 1-μm spatial resolution. The measurements indicate substantial reduction of the stress near the edges of 6-μm-wide structures.

A planar antenna has been designed which will serve as a subarray element in an imaging array intended for operation over the range 140 to 700 GHz. Scale-model measurements have been carried out at X-band which show that the radiation pattern of the antenna is suitable for such an array.

III. MATERIALS RESEARCH

In Si films prepared by zone-melting recrystallization of polycrystalline Si on SiO_2-coated fused quartz and sapphire substrates, the carrier mobilities are significantly influenced by stress which occurs because the thermal expansion coefficient of Si is much higher than that of fused quartz and less than that of sapphire. Because the films on SiO_2-coated fused quartz are under strong tensile stress, the electron Hall mobilities in these films are about 75-percent higher than those in films recrystallized on SiO_2-coated Si, and the electron mobilities in n-channel MOSFETs fabricated in the films on fused quartz are even higher than those in similar devices fabricated in bulk Si single crystals.

Single crystals of InP that are dislocation-free up to a diameter of about 20 mm have been grown by the liquid-encapsulated Czochralski technique, without impurity doping, by increasing the thickness of the B_2O_3 encapsulant layer to reduce the radial temperature gradients in the growing boule. X-ray topography and CO_2 laser transmission studies have shown that impurity-doped LEC crystals contain prominent growth striations, probably produced by random convection currents in the melt, that are associated with abrupt changes in dopant concentration.

The lateral vapor-phase epitaxial growth of InP over insulating films on (100) InP substrates has been studied as a function of orientation in the plane of the substrate. Significant lateral growth is found to occur for non-low-index directions because the growing layers are bounded by intersecting low-index facets that form corners which act as nucleation sites.

Good electrical activation of Se-implanted GaAs has been obtained by using a simple graphite strip-heater for transient annealing at temperatures between 900° and 1140°C. From the decrease in sheet resistivity and increase in sheet carrier concentration observed over this temperature range, it is probable that still better activation can be achieved by annealing at higher temperatures either with a better encapsulant or in an atmosphere with controlled arsenic vapor pressure.

Since the usefulness of transition-metal silicides for a variety of applications in Si integrated-circuit technology depends on their sensitivity to ion bombardment, sheet resistance measurements on polycrystalline films of seven silicides have been used to study the production of damage by Ar^+-ion bombardment. The sensitivity of the compounds to bombardment increases in the following order: Pd_2Si, Pt_2Si, PdSi, Ni_2Si, PtSi, NiSi, $NiSi_2$; the heat of formation per metal atom, which is believed to be correlated with the degree of covalent bonding, increases in the same order.

IV. MICROELECTRONICS

A novel etching technique has been developed which is similar to reactive ion etching, but allows the independent control of the energetic ions and the chemically reactive flux. The technique, called ion-beam-assisted etching (IBAE), provides high etching rates and the ability to etch a variety of structures. By using argon ions and a reactive flux of Cl_2, GaAs surfaces etched by IBAE can be made of sufficient quality for many device applications.

IBAE has been used to etch the channel for a recessed-gate, GaAs MESFET. A 250-μm-wide device with a 1.3-μm gate has a transconductance of 30 mS. This value of transconductance, which compares favorably with devices whose gate recess was etched by conventional techniques, indicates that IBAE has the potential to be an important processing technique for GaAs microwave devices.

V. ANALOG DEVICE TECHNOLOGY

Surface-acoustic-wave technology, which was recently used to demonstrate short-pedestal-of-delay filters, has been extended to provide wideband ($\approx$100-MHz) multipath simulators. Edge-bonded input transducers give both large (>1/2) fractional bandwidth and high (>100-dB) feedthrough isolation. Split-finger interdigital output transducers are apodized and random-phase encoded to provide a noise-like impulse response.

An elastic convolver with time-bandwidth product of 2200 has been demonstrated which incorporates a parabolic-horn acoustic beamwidth compressor for high efficiency (−69-dBm efficiency factor), a dual-track configuration with orthogonal transducers for self-convolution suppression (<−43 dB), a simplified output-combiner circuit for temporal uniformity (±0.5 dB, ±5°), and a chirped-transducer design for low spectral phase distortion (<±30°). This low-cost, compact device can provide programmable matched filtering of minimum-shift-keyed wideband spread-spectrum signals within 0.15 dB of ideal performance.

REPORTS ON SOLID STATE RESEARCH

15 September through 15 November 1981

PUBLISHED REPORTS

Journal Articles

JA No.

5152	Transition Temperatures and Heats of Crystallization of Amorphous Ge. Si. and $Ge_{1-x}Si_x$ Alloys Determined by Scanning Calorimetry	J. C. C. Fan C. H. Anderson. Jr.	J. Appl. Phys. **52**, 4003 (1981)
5186	Solid-Phase Epitaxial Crystallization of Amorphous Ge on ⟨100⟩ Si	B-Y. Tsaur J. C. C. Fan J. P. Salerno C. H. Anderson. Jr. R. P. Gale F. M. Davis E. F. Kennedy* T. T. Sheng*	J. Electrochem. Soc. **128**, 1947 (1981)
5200	Hydroplane Polishing of Semiconductor Crystals	J. V. Gormley M. J. Manfra A. R. Calawa	Rev. Sci. Instrum. **52**, 1256 (1981)
5218	Efficient Si Solar Cells by Low-Temperature Solid-Phase Epitaxy	B-Y. Tsaur G. W. Turner J. C. C. Fan	Appl. Phys. Lett. **39**, 749 (1981)
5219	GaAs Shallow-Homojunction Solar Cells on Ge-Coated Si Substrates	R. P. Gale J. C. C. Fan B-Y. Tsaur G. W. Turner F. M. Davis	IEEE Electron Device Lett. **EDL-2**, 169 (1981), DTIC AD-A107056
5222	Shallow PtSi-Si Schottky Barrier Contacts Formed by a Multilayer Metallization Technique	B-Y. Tsaur D. J. Silversmith R. W. Mountain L. S. Hung* S. S. Lau* T. T. Sheng*	J. Appl. Phys. **52**, 5243 (1981)
5240	Improved Techniques for Growth of Large-Area Single-Crystal Si Sheets Over SiO_2 Using Lateral Epitaxy by Seeded Solidification	B-Y. Tsaur J. C. C. Fan M. W. Geis D. J. Silversmith R. W. Mountain	Appl. Phys. Lett. **39**, 561 (1981)

---

* Author not at Lincoln Laboratory.

JA No.

5245	Mixing of 10-μm Radiation in Room-Temperature Schottky Diodes	P. E. Tannenwald H. R. Fetterman C. Freed C. D. Parker B. J. Clifton R. G. O'Donnell	Opt. Lett. $\underline{6}$, 481 (1981)
5246	Slider LPE of $Hg_{1-x}Cd_xTe$ Using Mercury Pressure Controlled Growth Solutions	T. C. Harman	J. Electron. Mater. $\underline{10}$, 1069 (1981)
5247	Remote Probing of the Atmosphere Using a CO_2 DIAL System	D. K. Killinger N. Menyuk	IEEE J. Quantum Electron. $\underline{QE-17}$, 1917 (1981)
5253	Direct Writing of Refractory Metal Thin Film Structures by Laser Photodeposition	D. J. Ehrlich R. M. Osgood, Jr. T. F. Deutsch	J. Electrochem. Soc. $\underline{128}$, 2039 (1981)

Meeting Speeches

MS No.

5230A	Picosecond Optical Sampling	H. A. Haus* S. T. Kirsch* K. Mathyssek* F. J. Leonberger	Proc. SPIE, Vol. 269: Integrated Optics (Society of Photo-Optical Instrumentation Engineers, Bellingham, Washington, 1981), pp. 55-59
5358A	The CLEFT Process: A Technique for Producing Epitaxial Films on Reusable Substrates	J. C. C. Fan C. O. Bozler R. W. McClelland	Proceedings of the Symposium on Materials and New Processing Technologies for Photovoltaics (The Electrochemical Society, Pennington, New Jersey, 1981), p. 304
5525	A New Technique for Preparing p-n Junctions for Si Photovoltaic Cells	J. C. C. Fan T. F. Deutsch G. W. Turner D. J. Ehrlich R. L. Chapman R. M. Osgood, Jr.	Proc. Fifteenth IEEE Photovoltaic Specialists Conference – 1981, Orlando, Florida, 12-15 May 1981, pp. 432-436
5531	GaAs Shallow-Homojunction Solar Cells on Epitaxial Ge Grown on Si Substrates	R. P. Gale B-Y. Tsaur J. C. C. Fan F. M. Davis G. W. Turner	Proc. Fifteenth IEEE Photovoltaic Specialists Conference – 1981, Orlando, Florida, 12-15 May 1981, pp. 1051-1055
5532	Cathodoluminescence Analysis of Polycrystalline GaAs	J. P. Salerno R. P. Gale J. C. C. Fan	Proc. Fifteenth IEEE Photovoltaic Specialists Conference – 1981, Orlando, Florida, 12-15 May 1981, pp. 1174-1178
5533	GaAs Shallow-Homojunction Concentrator Solar Cells	G. W. Turner J. C. C. Fan R. L. Chapman R. P. Gale	Proc. Fifteenth IEEE Photovoltaic Specialists Conference – 1981, Orlando, Florida, 12-15 May 1981, pp. 151-155

* Author not at Lincoln Laboratory.

---

* Author not at Lincoln Laboratory.

UNPUBLISHED REPORTS

Journal Articles

JA No.

5209	Solar Photovoltaic Cells	J. C. C. Fan	Accepted by Kirk-Othemer Encyclopedia of Chemical Technology
5244	Optical Technique for Measurements of Submonolayer Adsorbed Films	V. Daneu R. M. Osgood, Jr. D. J. Ehrlich	Accepted by Opt. Lett.
5249	Laser Microreaction for Deposition of Doped Silicon Films	D. J. Ehrlich R. M. Osgood, Jr. T. F. Deutsch	Accepted by Appl. Phys. Lett.
5261	Techniques for Electron Beam Testing and Restructuring Integrated Circuits	D. C. Shaver	Accepted by J. Vac. Sci. Technol.
5262	A Novel Anisotropic Dry Etching Technique	M. W. Geis G. A. Lincoln N. Efremow W. J. Piacentini	Accepted by J. Vac. Sci. Technol.
5263	Sub-Doppler Submillimeter Spectroscopy Using Molecular Beams	W. A. M. Blumberg D. D. Peck H. R. Fetterman	Accepted by Appl. Phys. Lett.
5264	Cryogenic Operation of Submillimeter Quasioptical Mixers	P. F. Goldsmith* H. R. Fetterman B. J. Clifton C. D. Parker N. R. Erickson*	Accepted by Intl. J. Infrared and Millimeter Waves
5269	The Permeable Base Transistor and Its Application to Logic Circuits	C. O. Bozler G. D. Alley	Accepted by Proc. IEEE
5270	Production and Annealing of Ion-Bombardment Damage in Silicides of Pt, Pd and Ni	B-Y. Tsaur C. H. Anderson, Jr.	Accepted by J. Appl. Phys.
5276	N-Channel Deep-Depletion MOSFETs Fabricated in Zone-Melting-Recrystallized Polysilicon Films on SiO_2	B-Y. Tsaur M. W. Geis J. C. C. Fan D. J. Silversmith R. W. Mountain	Accepted by Appl. Phys. Lett.
5279	Zone-Melting Recrystallization of Encapsulated Silicon Films on SiO_2 – Morphology and Crystallography	M. W. Geis H. I. Smith* B-Y. Tsaur J. C. C. Fan E. W. Maby* D. A. Antoniadis	Accepted by Appl. Phys. Lett.

* Author not at Lincoln Laboratory.

JA No.

| 5291 | Electrical Properties of Laser Chemically Doped Silicon | T. F. Deutsch
D. J. Ehrlich
D. D. Rathman
D. J. Silversmith
R. M. Osgood, Jr. | Accepted by Appl. Phys. Lett. |

Meeting Speeches[*]

MS No.

5608A	Comparative Sensitivity of Dual-Laser and Single-Laser Remote Sensing of Atmospheric Species	D. K. Killinger N. Menyuk	1981 Annual Optical Society of America Mtg., Kissimmee, Florida, 26-30 October 1981
5707D	Microreactions Using Laser Beams	D. J. Ehrlich R. M. Osgood, Jr. T. F. Deutsch	
5653A	Linewidth Characteristics of (GaAl)As Semiconductor Diode Lasers	A. Mooradian D. Welford M. W. Fleming	Workshop on "Optical Processing Elements," London, England, 17-18 September 1981
5695	SAW Convolvers for Spread-Spectrum Communications	L. Yao	1981 Natl. Electronics Conf., Chicago, Illinois, 26-28 October 1981
5707B	Laser Microchemistry for Electronics	D. J. Ehrlich R. M. Osgood, Jr. T. F. Deutsch	Fifth Intl. Thin Films Congress, Herzlia-on-Sea, Israel, 21-25 September 1981
5707C	Laser Photodeposition	D. J. Ehrlich R. M. Osgood, Jr. T. F. Deutsch	Amer. Vac. Soc. Natl. Symp., Anaheim, California, 3-6 November 1981
5707E	Laser Microphotochemistry for Electronics	D. J. Ehrlich R. M. Osgood, Jr. T. F. Deutsch	IEEE Local Chapter Mtg., Waltham, Massachusetts, 14 October 1981
5717A	High Quality MOSFETs on Silicon Films Prepared by Zone-Melting Recrystallization of Encapsulated Polysilicon on SiO_2	B-Y. Tsaur	Seminar, Hughes Research Laboratory, Malibu, California, 24 July 1981
5717B	Growth of Large-Area Device-Quality Si Sheets on Insulators	B-Y. Tsaur	Materials Science and Engineering Seminar, Cornell University, Ithaca, New York, 10 September 1981
5717C	Preparation of High-Quality Silicon Films on Insulators by Zone-Melting Recrystallization	B-Y. Tsaur	Seminar, RCA, Princeton, New Jersey, 1 October 1981

[*]Titles of Meeting Speeches are listed for information only. No copies are available for distribution.

ORGANIZATION

SOLID STATE DIVISION

A. L. McWhorter, *Head*
I. Melngailis, *Associate Head*
J. F. Goodwin, *Assistant*

P. E. Tannenwald, *Senior Staff*

QUANTUM ELECTRONICS

A. Mooradian, *Leader*
P. L. Kelley, *Associate Leader*

Barch, W. E.
Belanger, L. J.
Brueck, S. R. J.
Burke, J. W.
Bushee, J. F.
Clabasey, C.*
Coulombe, M. J.
Daneu, V.
DeFeo, W. E.
Deutsch, T. F.
Ehrlich, D. J.
Feldman, B.
Fetterman, H. R.

Goodhue, W. D.*
Hancock, R. C.
Johnson, B.*
Killinger, D. K.
Lewis, R. C.*
Menyuk, N.
Moulton, P. F.
Murphy, D. V.
Parker, C. D.
Peck, D. D.
Sullivan, D. J.
Welford, D.

ELECTRONIC MATERIALS

A. J. Strauss, *Leader*
H. C. C. Fan, *Assistant Leader*
J. G. Mavroides, *Senior Staff*
H. J. Zeiger, *Senior Staff*

Anderson, C. H., Jr.
Button, M. J.
Chapman, R. L.
Davis, F. M.
Delaney, E. J.
Fahey, R. E.
Finn, M. C.
Foley, G. H.
Gale, R. P.
Iseler, G. W.
Kolesar, D. F.
Krohn, L., Jr.

Mastromattei, E. L.
Metze, G. M.
Nitishin, P. M.
Owens, E. B.
Palm, B. J.
Pantano, J. V.
Salerno, J. P.*
Tracy, D. M.
Tsaur, B-Y.
Turner, G. W.
Vohl, P.

APPLIED PHYSICS

R. C. Williamson, *Leader*
C. E. Hurwitz, *Associate Leader*
T. C. Harman, *Senior Staff*
R. H. Kingston, *Senior Staff*
R. H. Rediker, *Senior Staff*

Armiento, C. A.*
Becker, R. A.
Calawa, A. R.
Carter, F. B.
Chinnock, C. B.
DeMeo, N. L., Jr.
Diadiuk, V.
Donnelly, J. P.
Ferrante, G. A.
Foyt, A. G.
Groves, S. H.
Hovey, D. L.
Johnson, L. M.*
Lattes, A. L.*

Leonberger, F. J.
Liau, Z. L.
Lind, T. A.
Manfra, M. J.
McBride, W. F.
O'Donnell, F. J.
Orr, L.*
Paladino, A. E.
Plonko, M. C.
Schloss, R. P.*
Spears, D. L.
Tsang, D. Z.
Walpole, J. N.
Woodhouse, J. D.†

ANALOG DEVICE TECHNOLOGY

E. Stern, *Leader*
J. H. Cafarella, *Assistant Leader*
R. W. Ralston, *Assistant Leader*

Anderson, A. C.
Arsenault, D. R.
Baker, R. P.
Behrmann, G. J.
Brogan, W. T.
DiPerna, M. S.‡
Dolat, V. S.
Fischer, J. H.
Flynn, G. T.
Holtham, J. H.
Kernan, W. C.

Leung, I.
Lowney, S. D.
Lynch, J. T.‡
Macedo, E. M., Jr.
Macropoulos, W.
Oates, D. E.
Reible, S. A.
Slattery, R. L.
Withers, R. S.
Wright, P. V.
Yao, I.

MICROELECTRONICS

W. T. Lindley, *Leader*
F. J. Bachner, *Associate Leader*
N. P. Economou, *Assistant Leader*
R. A. Murphy, *Assistant Leader*

Alley, G. D.
Bozler, C. O.
Bromley, E. I.
Burke, B. E.
Cabral, S. M.
Chiang, A. M.
Chu, A.
Clifton, B. J.
Daniels, P. J.
DeGraff, P. D.

Dryden, C. D.
Durant, G. L.
Efremow, N. N., Jr.
Elta, M. E.
Felton, B. J.
Flanders, D. C.
Geis, M. W.
Goeloe, G. T.†
Gray, R. V.
Hansell, G. L.*

Lincoln, G. A., Jr.
Lyszczarz, T. M.
Mahoney, L. J.
McClelland, R. W.
McGonagle, W. H.
Melngailis, J.‡
Mountain, R. W.
Mroczkowski, I. H.
Nichols, K. B.
Pang, S.

Piacentini, W. J.
Pichler, H. H.
Rabe, S.
Rathman, D. D.
Shaver, D. C.
Silversmith, D. J.
Smythe, D. L., Jr.
Vigilante, J. L.
Vojak, B. A.
Wilde, R. E.

* Research Assistant
† Staff Associate
‡ Part Time

I. SOLID STATE DEVICE RESEARCH

A. EXTERNAL-CAVITY CONTROLLED OPERATION OF A SEMICONDUCTOR-DIODE GAIN ELEMENT IN SERIES WITH AN OPTICAL FIBER

The series combination of a semiconductor-diode gain element (a diode laser whose end facets have been antireflection coated) and an optical fiber has been placed inside an external cavity as illustrated in Fig. I-1. The external cavity operated with an output at a single wavelength whose width was less than the 1.7×10^{-5}-nm resolution of the scanning Fabry-Perot interferometer used. The spectrum illustrated in Fig. I-2(a-b) is for a multimode optical fiber inside the cavity, as illustrated in the inset in the figure. When a grating in the Littrow configuration is used as one of the cavity end reflectors, the spectral line can be tuned. A polarizer has also been placed inside the cavity at the fiber output to select the polarization of this output. With proper alignment of the elements inside the cavity, temporally stable operation of the external-cavity output is obtained. The output as measured with a wide-bandwidth photodetector circuit was displayed on an oscilloscope, and there were no spikes or fluctuations within the limiting 225-MHz bandwidth of the oscilloscope. The output (approximately 1 mW) was measured using a spectrum analyzer with system noise of 10 nW within any 300-kHz-bandwidth interval. No noise above this level was measurable up to 100 MHz and at the cavity mode-beat frequency of 280 MHz. The drift in the output which occurs over the order of several minutes is consistent with thermal variations expected in the experiment. Figure I-3 illustrates the stability as measured over a period of 1 min. by taking 13 Fabry-Perot interferometer scans each 5 s apart. The results shown in this figure are for a single-mode fiber in the cavity.
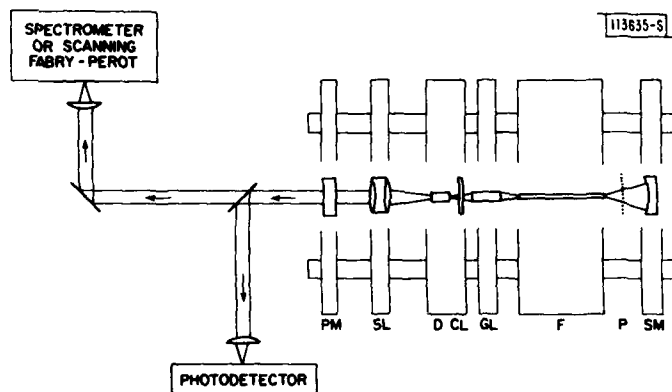
Fig. I-1. Optical layout of experiments. External-cavity laser components are shown in a top, cutaway view through four-bar Super-Invar supporting structure. Labeled elements are: PM — plane mirror; SL — spherical collimating lens; D — diode gain element; CL — 40-mm-dia. cylindrical lens; GL — graded-index (GRIN) rod lens; F — 14-cm-long optical fiber; P — polarizer; SM — spherical mirror. Polarizer was removed for some experiments. Plane mirror (PM) was replaced by a grating in Littrow configuration in other experiments (output in this case was zero order of grating).

1
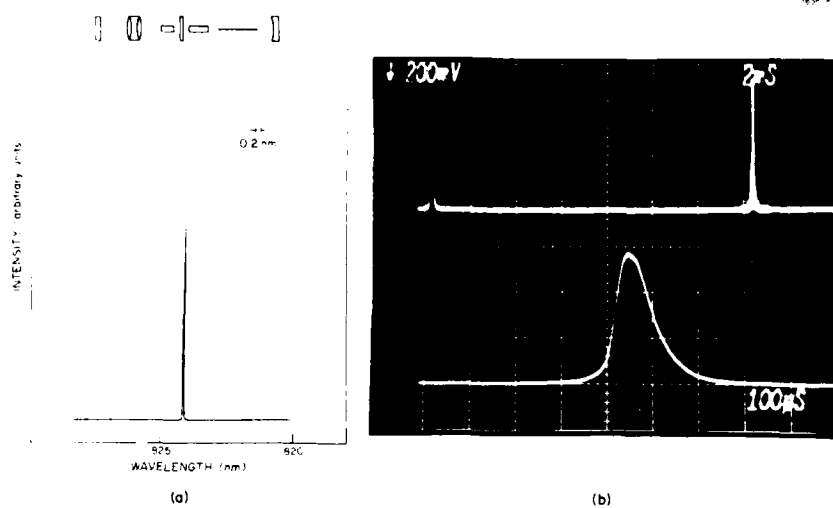
Fig. I-2. (a) Spectrum of stimulated emission output of external cavity containing series combination of a diode gain element and a multimode fiber. (b) Fabry-Perot scan of this spectrum. Top trace shows entire 1500-MHz free spectral range; bottom trace shows that FWHM of line is indistinguishable from 7.5-MHz instrument resolution. These results are typical for output powers up to 2-mW level set by diode life considerations.
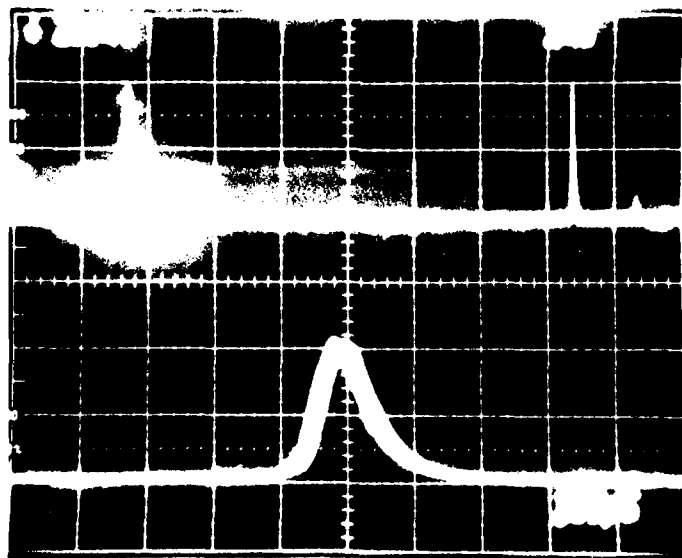
Fig. I-3. Measurement of stability of laser over a 1-min. time interval. Traces are made up of 13 Fabry-Perot scans of spectrum, each taken 5 s apart. As in Fig. I-2, top trace shows entire 1500-MHz free spectral range, and abscissa is expanded by a factor of 20 in bottom trace. For results illustrated, external cavity contained series combination of a diode gain element and a single-mode fiber.

2

Similar results have been obtained with either a single-mode or multimode fiber in the cavity. The values of the threshold for stimulated emission have been measured, and a model has been developed to use these values and others obtained by diagnostic measurements in determining the insertion loss (including the coupling inefficiency) of the fibers. While the multimode fiber collects approximately 70 percent and the single-mode fiber approximately 20 percent of the radiation from the diode gain element (and in similar experiments from a diode laser from the same batch), the insertion loss of the multimode fiber is nearly the same as that of the single-mode fiber. This result is expected because only a selected mode (or selected modes) of the multimode fiber can participate in the laser action of the external cavity.

The results obtained in this work are consistent with results reported for an external cavity without a fiber.[1] The temporal and/or spectral results obtained differ, however, from results reported for the combination of a diode laser and a fiber used as an external cavity.[2,3] The stable CW operation we have described was achieved when we appropriately aligned the elements inside our cavity.

The experiments reported here are aimed toward demonstrating the feasibility of coupling semiconductor-diode lasers in parallel by using optical fibers and thus verifying the concept of a laser system with average power up to the order of kilowatts (see Fig. 1-4). The fibers are required so that the diode lasers (actually gain elements) can be used in subgroups "remote" from the cavity to reduce the density of the power that has to be dissipated. Since the electromagnetic mode of a semiconductor-diode gain element (laser) is TE and the electromagnetic mode of an optical fiber is HE, both different from the free-space mode, it was important to make certain that the combination of semiconductor-diode gain element and optical fiber performed appropriately in an external cavity. The results presented above demonstrate that this combination does perform appropriately.

R. H. Rediker   A. Mooradian
R. P. Schloss   D. Welford
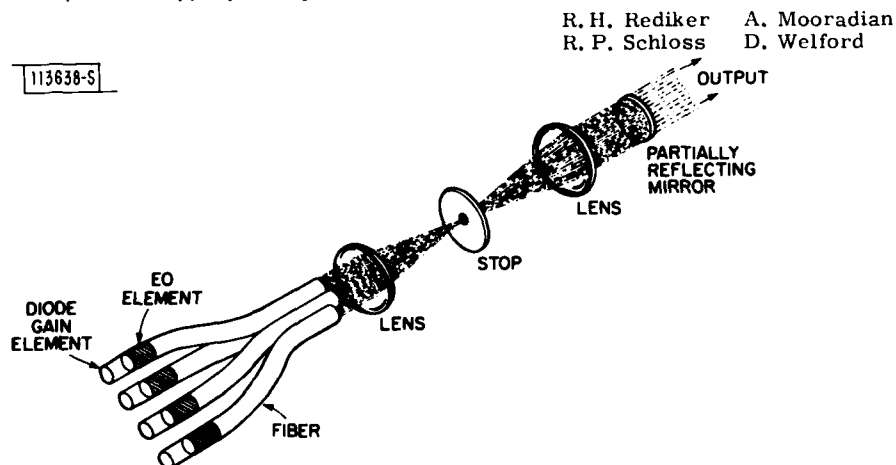
Fig. 1-4. Concept of fiber-coupled external-cavity semiconductor high-power laser illustrating from left-to-right: semiconductor-diode gain element whose left facet is coated for near unity reflectivity, and whose right facet is anti-reflection coated; electrooptic element for phase shifting; focusing lens; appropriate spatial filter to assure coherence of wavefront across entire fiber bundle emitter (illustrated schematically as a stop); focusing lens to recollimate beam; and a partially reflecting mirror. External cavity is bounded on left by reflecting facets of semiconductor gain elements, and on right by partially reflecting mirror.

B. PICOSECOND InP OPTOELECTRONIC SWITCHES

Experiments have been carried out to show that proton bombardment reduces the response times of InP optoelectronic switches from ~5 ns to <100 ps. *The electron mobility in these bombarded devices can be as large as 1000 cm^2/V-s, over an order of magnitude larger than that of devices of comparable speed made on other high-resistivity materials.*[4-6] In addition, the characteristics of these new switches are compared with those of the previously reported InP switches.[7]

The devices were fabricated on slices of semi-insulating InP that had a resistivity of ~5 × 10^7 Ω-cm and a bulk mobility of ~2500 to 3500 cm^2/V-s. Following conventional polishing and etching procedures, interdigital-finger electrode structures of Au/Ge/Ni were patterned onto the InP using vacuum evaporation and lift-off lithography. The devices investigated here had 2-μm-wide fingers and spaces with an overall active area of 48 × 48 μm, as illustrated in Fig. I-5.
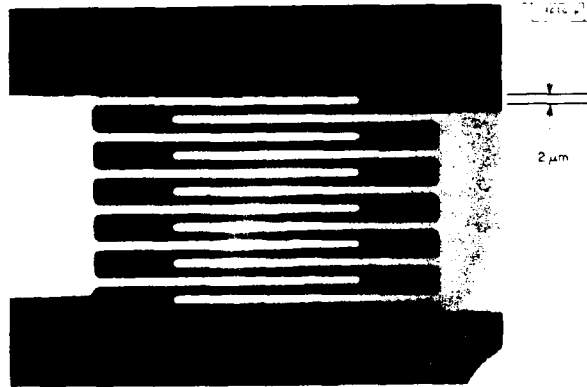
Fig. I-5. Photograph of InP optoelectronic switch. Interdigital electrode lines and spaces are 2 μm wide, and overall active area is 48 × 48 μm.

After the electrodes had been patterned, the slice was cleaved into five separate pieces, with each piece having several devices of the 2-μm geometry, as well as other devices of 4- and 6-μm geometry. The latter devices were examined only briefly. Each piece was covered with pyrolytic phosphosilicate glass (PSG) and annealed at 450°C for 10 s. The glass was then removed, one piece set aside as a standard, and the remaining four were bombarded with a 10^{13} cm^{-2} dose of 200-keV protons. Three of these samples were then annealed in hydrogen: one at 250°C, one at 300°C, and one at 350°C — each for 10 s. Each sample was then cem ted to a grooved aluminum block and wire bonded to OSM connectors for evaluation.

Preliminary low-speed measurements were done using a raster-scanned He-Ne laser light spot to insure that these devices had the uniformity of photoresponse, linearity of current-voltage characteristics, and the near-theoretical sensitivity of earlier devices.[8-9] High-speed photoresponse measurements were done using as a pulsed light source a commercial low-threshold AlGaAs diode laser (λ ~ 0.85 μm), driven by a commercial impulse train generator.[10] The light pulses have a repetition rate of 100 MHz and a full width at half maximum of ~100 ps,

as measured by an InP/GaInAsP/InP n^+-n-p^+ photodiode fabricated at Lincoln Laboratory. The peak optical power focused on the device was estimated to be 3 mW.

The results are shown in Figs. I-6(a-b) and I-7(a-c). For the unbombarded device, the fall time of the photoresponse is approximately exponential with a 90- to 10-percent fall time of ~5 ns (time constant ~2.3 ns). Also, from a previous study of device resistance as a function of finger geometry, the electron mobility is estimated to be ~2000 cm^2/V-s. Following bombardment, both the response time and mobility were substantially reduced, with the rise and fall times each <100 ps and electron mobility of ~200 cm^2/V-s. Following bombardment and the 250°C anneal, the rise and fall times remained at <100 ps, but the mobility recovered to at least 1000 cm^2/V-s. The mobility recovery was estimated by the amplitude of the photoresponse compared with that of the unbombarded device. This measurement may underestimate the mobility value because of carrier recombination during the light pulse. Also, a small "back porch" on the trailing edge of the response is apparent. Finally, with increasing anneal temperature, the fast component of the rise and fall times remains at <100 ps, and the mobility remains at 1000 cm^2/V-s. However, the back-porch component increases in magnitude as the device is annealed toward its unbombarded state. The shape of these pulses was insensitive to focusing and total light incident on the device.

Another effect of the bombardment that may be a limitation in some cases is a decrease in the off-state (dark) resistance. For the device that was bombarded and annealed at 250°C, the off-state resistance decreased from >10 MΩ to ~50 kΩ. This value can be compared with the on-state value of ~500 Ω in the present experiment, and an anticipated value of <50 Ω when the laser is replaced with one having greater output power. Also, it is not clear at this time that the off-state resistance decrease is a necessary result of proton bombardment. More work with different bombardment and anneal schedules, and perhaps with other ions, is currently under way to investigate this effect. It is also worth noting that since higher proton doses increase absorption below the band edge,[11] it may be possible to extend the wavelength dependence of these devices to ≥1 μm.

It is interesting to compare the present results with the earlier fast InP optoelectronic switch.[7] In that case, the devices were fabricated on InP slices similar to those used here, but the metallization was vacuum-evaporated gold that was patterned using conventional photolithography and wet chemical etching into a 30-μm-wide microstrip line with a 3-μm gap in the middle of its length. That device had a 1- to 2-ns response time as originally fabricated. However, by using a short anneal (~10 s) in hydrogen at 400°C, it was possible to reproducibly reduce this response time to ~50 ps. However, our attempts to apply this technique to the present alloyed-contact higher-response devices have not been successful. It is worth noting, however, that the current devices have substantially lower contact resistance and are nearly immune from photovoltaic effects, which suggests that the fast response of earlier devices may be associated with photovoltaic effects. Because of this success of the bombardment technique, we are currently pursuing it instead of further research on the heat-treatment technique.

In summary, InP optoelectronic switches have been fabricated which have fast response times (<100 ps) and high electron mobility (~1000 cm^2/V-s) following proton bombardment and anneal. Work is currently in progress to optimize response time and mobility while minimizing the off-state conductance. These devices are well suited for high-speed sampling and mixing applications, especially in those situations which require the absence of a DC offset and/or the
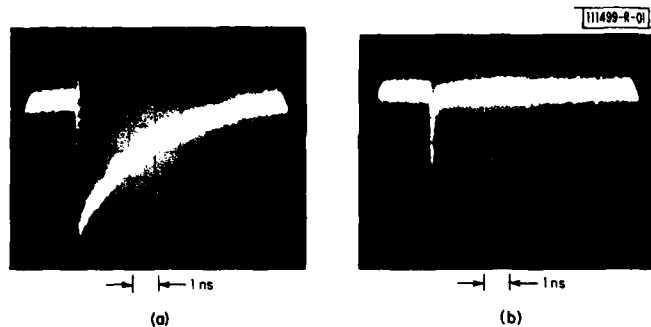
Fig. I-6. Photoresponse of InP optoelectronic switches to short pulses
(<100 ps) of AlGaAs diode laser ($\lambda \sim$ 0.85 μm) with 3-mW peak power.
DC voltage of 300 mV was connected between ground and one terminal
of device, with response shown observed between other terminal and
ground on a high-speed sampling oscilloscope (response time $\sim$ 25 ps).
(a) Unbombarded device; (b) device bombarded with a 10^{13} cm^{-2} dose
of 200-kV protons and subsequently annealed at 250°C for 10 s.
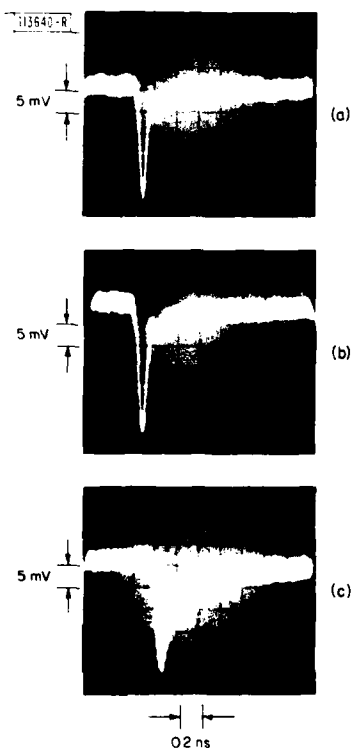
Fig. I-7. Photoresponse of three InP
optoelectronic switches described in
Fig. I-6, following proton bombard-
ment and subsequent 10-s anneal at:
(a) 250°C, (b) 300°C, and (c) 350°C.

6

high degree of isolation between the local oscillator and output that this device offers. Other applications such as optical detection could simply make use of the high speed of these devices.

<div align="right">

A. G. Foyt   R. C. Williamson
F. J. Leonberger   G. W. Iseler

</div>

C. DIFFUSION LENGTH OF HOLES IN n-InP

Hole diffusion lengths of 12 μm in n-InP have been determined by measuring the increase in collection efficiency of an InP photodiode as a function of reverse bias. This diffusion length is much greater than the previously reported value measured on this material by a surface photovoltage technique.[12]

The devices investigated in this study were InP p^+-n-n^+ inverted-mesa structures fabricated using LPE growth and photolithographic techniques.[13] The structure and device parameters are shown in Fig. I-8. The thin (≤ 0.5 μm) n^+ cap layer serves to reduce surface recombination and band-bending effects observed in n-type InP,[†] but does not significantly reduce the quantum efficiency of the device. For reasons to be discussed below, the thickness d of the n-type InP layer was 5, 16, and 30 μm in the three different wafers tested. The devices were passivated with polyimide,[13] and an evaporated Au mask covering the mesa sides was applied to the finished devices. This mask prevented any light from being incident on the exposed depletion region at the mesa sides, thus insuring that the measured photocurrent is due only to the holes that have diffused to the depletion region after photogeneration near the top surface.

Fig. I-8. InP avalanche photodiode structure and parameters. Diameter was 5, 16, and 30 μm for various devices. Au edge-mask is to prevent light incident on mesa sides.
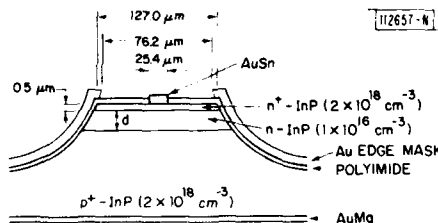
By fitting both the magnitude and functional form of the low-bias region of the AC photocurrent vs voltage characteristics $I_p(V)$ to the current predicted by a model including diffusion and surface recombination, it is possible to determine the diffusion length L_p and surface recombination velocity $\underline{s}$. The theory takes into account the increase in collection efficiency due to the widening of the depletion region with increasing reverse bias, but does not include avalanche multiplication. Thus, it applies only to the low-bias portion of $I_p(V)$. Figure I-9 shows the voltage dependence of the photocurrent measured before and after masking the side of a device, together with the theoretically predicted unmultiplied photocurrent. Without the edge-mask, the measured photocurrent rises very rapidly because of the direct injection into the increasingly wider depletion region. When this curve is fitted, the result is an artificially low value of L_p, because the entire increase in photocurrent is ascribed to depletion region widening.

---

† The surface effects observed in n-type InP include a nonlinear dependence of the output photocurrent on the incident laser power, most likely due to a dead space at the surface resulting from trapping or recombination centers. This will be reported in detail later.
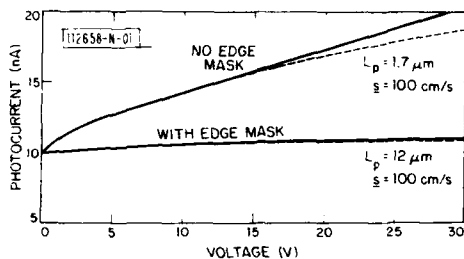
Fig. I-9. Theoretical and experimental photocurrent $I_p(V)$ as a function of bias voltage with and without edge mask. Values of L_p and $\underline{s}$ correspond to best theoretical fit to experimental data. Bias at which experimental data depart from theory corresponds to onset of avalanche multiplication.

When the device is properly masked so that the photocurrent is due entirely to light incident from the top, an unambiguous measurement can be made. By fitting the voltage dependence and magnitude of the experimentally measured photocurrent, accurate values of L_p and $\underline{s}$ can be obtained.

By using samples of three different n-layer thicknesses, it was possible to confirm the accuracy of the technique and reproducibility of the results over a wide range of values of quantum efficiency (11 to 60 percent). Testing diodes with very thick n-type layers is important because only when $d > L_p$ is the voltage dependence of the photocurrent sufficiently strong to give a sensitive measure of L_p. Using this technique, a consistent set of parameters yielding $L_p \sim 12 \ \mu m$ and $\underline{s} \sim 100$ cm/s was obtained for samples with $d \approx 0.4 \ L_p$, $d \approx 1.3 \ L_p$, $d \approx 2.5 \ L_p$.

This value of $\underline{s}$ is in agreement with that obtained from photoluminescence.[14] However, the value of L_p obtained from the fitting procedure is in disagreement with both the published photovoltage data[12] and the value of 1 to 2 μm determined by electron-beam-induced-current (EBIC) measurements carried out on the same devices. (Our EBIC data are in agreement with published EBIC results.[15]) The likely reason for this discrepancy with respect to the surface photovoltage data is that those measurements are carried out on n-type InP (with no n^+ cap layer) and can be, therefore, seriously affected by the surface band-bending effects present in moderately doped InP. In the case of measurements using EBIC, the discrepancy is due to the fact that the EBIC technique is not quantitatively valid unless the e-beam penetration depth is at least several diffusion lengths,[16] so that carrier recombination at the cleaved surface upon which the electrons are incident can be neglected. The interpretation of the EBIC data is further complicated unless the distance of the junction from the n^+ surface is also several diffusion lengths. Clearly, neither of these conditions is satisfied here. On the other hand, the photocurrent measurements yield the bulk value of L_p, since the n^+ cap layer largely eliminates surface losses, and the holes, generated near the surface, diffuse through the entire n-layer before being collected.

Assuming a hole diffusion constant of 4 cm^2/s, a minority carrier lifetime of ~360 ns can be calculated from the measured diffusion length. To independently verify this value, transient photoconductivity experiments were carried out.[†] Though not a direct confirmation, since these measurements were made at high-injection levels as opposed to the low-injection regime of the photocurrent experiments, the results obtained were consistent with lifetimes on the order of several hundreds of nanoseconds. These results are also in agreement with the values of the carrier lifetime recently obtained from measurements of the modulation frequency response of the spontaneous emission in semiconductor laser structures.[17]

V. Diadiuk   S. H. Groves
C. A. Armiento   C. E. Hurwitz

[†] In collaboration with S. R. J. Brueck.

8

D. 4-BIT 275-MS/s GUIDED-WAVE ELECTROOPTIC ANALOG-TO-DIGITAL CONVERTER

The initial demonstration of a 4-bit 275-MS/s guided-wave electrooptic A/D converter is reported. The device consists of a mode-locked Nd:YAG laser, an array of Ti-diffused $LiNbO_3$ interferometric modulators, a Ge avalanche photodiode, and a special high-speed Si integrated circuit. This converter is of a type originally proposed by Taylor.[18] It depends on the periodic variation of the output of a guided-wave interferometric modulator with both voltage and electrode length to perform the conversion and the availability of short optical pulses from mode-locked lasers to perform the analog sampling. The Si integrated circuit acts as a comparator and serial-to-parallel converter. Two detailed studies of the design considerations for this A/D converter, as well as a number of reports of fundamental modulator experiments,[19-21] have been reported.[22,23] There have also been reports[24,25] of optical A/D converters which operated at higher drive powers and at either lower speed or bit number than the device reported here.
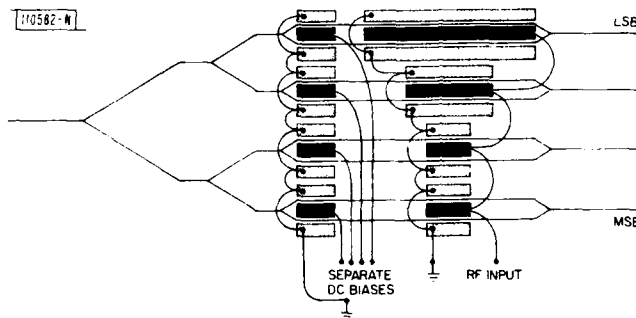
Fig. I-10. Schematic diagram of $LiNbO_3$ guided-wave interferometer array for electrooptic A/D converter. Waveguides are shown by thin lines. Separate DC biases can be applied to each modulator, and RF signal is applied to all modulators in parallel.

The $LiNbO_3$ device we have developed is shown schematically in Fig. I-10. It consists of four parallel interferometric modulators fed from a common input via a multiple-branching circuit. Each interferometer has DC-bias electrodes to adjust for any imbalance in the interferometers. The RF signal to be digitized is applied to the four modulators. The modulator electrodes for three devices differ in length by factors of two. The longest electrodes are 18 mm and correspond to the least-significant bit (LSB). Gray code output is obtained by making the electrodes for the two shortest modulators identical and by applying a DC bias equivalent to a $\pi/2$ phase shift to one of the identical modulators. By aligning the electrodes along a common centerline, conversion errors due to differential delay between the bits can be minimized.[23] The optical waveguides are 6-μm wide and designed for single-mode operation at a wavelength of 1.06 μm. The $LiNbO_3$ crystals are X-cut with Y-propagation, and TE polarization is used to take advantage of the large r_{33} electrooptic coefficient. The measured V_π voltage was 2.1 V for the longest modulator, so that a peak voltage of 8.4 V is required to operate a 4-bit accuracy. The overall chip length was 6 cm, and endfire coupling was used to test the device.
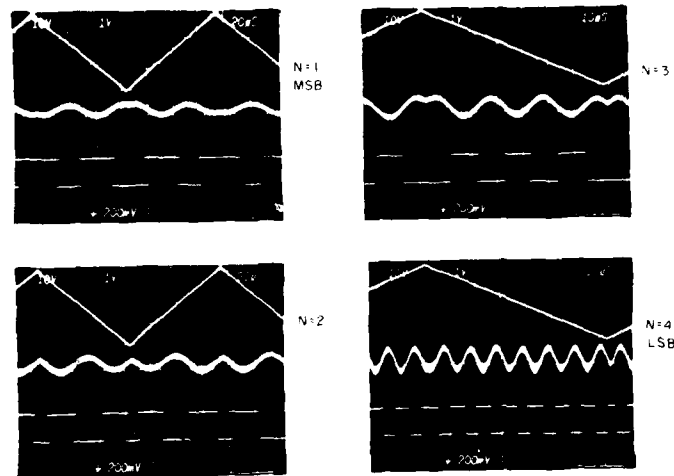
Fig. I-11. Response to a ramp drive of four different bit channels of electrooptic A/D converter. In each oscillogram, top trace is ramp drive, middle trace is modulator output, and bottom trace is corresponding comparator output.

(a)

(b)
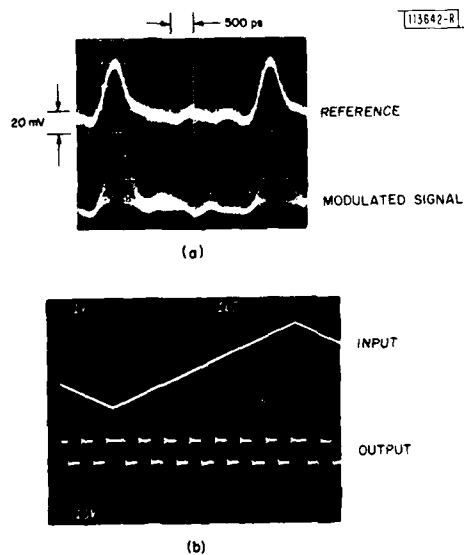
Fig. I-12. (a) Reference- and signal-channel comparator inputs at 276 MHz. The 200-ps-wide mode-locked optical pulses are broadened by Ge APD and amplifier. (b) A/D converter response to ramp drive at a 276-MHz sampling.

10

The mode-locked Nd:YAG laser generates a train of 200-ps-wide pulses at a 275-MHz rate. The input branching circuit consists of a set of 2 Y-splitters and isolated 4 bends. Interferometers similar to but much shorter than those used here have been reported with a 25-dB extinction ratio.[26] The comparators are integrated on a Si IC with an 8 1 serial-to-parallel converter so that the high-speed bit output can be slowed to a more conventional bit rate. This IC has successfully operated at 1 GHz (Ref. 27).

A variety of tests have been performed on this device. Figure 1-11 shows the detected Gray-code outputs from each of the four interferometers for a common CW optical input and a ramp drive signal. The comparator outputs are also shown. As can be seen, variations of the outputs are periodic and symmetric with respect to the ramps and differ in frequency by a factor of two as expected, except for the most-significant bit (MSB), where only a $\pi/2$ phase shift has been introduced.

Initial high-speed measurements were made using a single-bit channel output circuit consisting of a Ge avalanche photodiode, a wideband amplifier, and the high-speed Si comparator/serial-to-parallel converter chip. Figure 1-12(a-b) shows oscillograms of the sampled time-synchronized reference and signal inputs to the comparator. The reference signal was obtained by detecting a portion of the mode-locked pulse power with a second Ge APD. The filled-in signal envelope is due to modulation applied to the interferometers. The comparator output for a ramp drive signal applied to the LSB modulator is shown in Fig. 1-12(b). It is important to note that even though the comparator is toggling at a relatively low speed in response to the ramp, comparisons are being made at a 275-MHz rate.

BEAT FREQUENCY (1 MHz)

DETECTOR OUTPUT

COMPARATOR OUTPUT

INPUT SIGNAL 139 MHz, 32 dBm
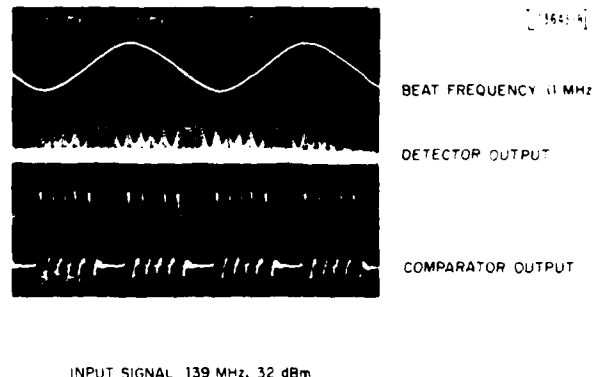
Fig. 1-13. Beat-frequency test of electrooptic A/D converter. Input RF signal is at 139 MHz; sampling is at 275 MHz. Shown are beat signal, as derived from an electronic mixer, and detector and comparator outputs. Relative phase of beat signal has not been synchronized to that of detector and comparator.

The oscillogram in Fig. 1-13 shows results of a beat-frequency test, a common test for high-speed A/D converters. In one version of this test, an RF sinusoid is applied to the converter at a frequency slightly offset from one-half the sampling-pulse-train frequency. The converter effectively mixes these two frequencies and allows the high-frequency operation of the device to be monitored at the significantly lower offset frequency. In our case a 139-MHz

signal is applied to the modulators along with the 276-MHz optical pulse train to generate a
1-MHz beat frequency. This beat frequency, as derived separately from an electronic mixer,
is displayed in the upper trace, the expected FM-modulated interferometer output is shown in
the middle trace, and the comparator output is shown in the lower trace. The comparator is
again functioning at 275 MHz. Further tests on this device are in progress, including tests with
a higher sampling rate.

F. J. Leonberger
C. E. Woodward
R. A. Becker

E. WIDE-BANDWIDTH 30-μm HgCdTe PHOTODIODES

Planar Hg-diffused HgCdTe photodiodes operating at 20 K with cutoff wavelengths of over
30 μm have shown response times of less than 0.6 ns at 20 μm. These devices are being de-
veloped for use as wide-bandwidth heterodyne receivers at 28 μm (the wavelength of a molecular
hydrogen transition) for astrophysical applications. For a 1-GHz photomixer bandwidth, photo-
diodes should have a 28-μm local oscillator power requirement of less than 50 μW (about 1 per-
cent of that required for a photoconductor) to be compatible with diode laser power levels.

The long-wavelength photodiodes were fabricated by a previously described[28] planar process
using an RF-sputtered ZnS diffusion mask on well-characterized bulk HgCdTe wafers with a
CdTe alloy composition of about 17.6 percent. Two different-size devices were made with active
area diameters of 90 and 190 μm. Prior to fabrication, two-zone anneals[29] in Hg vapor were
carried out to adjust the acceptor concentration of the HgCdTe wafers to about 7×10^{16} cm^{-3}.
This hole concentration affects the lifetime of the minority electrons,[30] their diffusion length,
and the conductivity of the p-type region of the photodiode. Prior to the device fabrication, the
annealed material was examined by room-temperature optical transmission measurements in
order to establish the precise energy of the exponential absorption edge tail.[31] This measure-
ment, along with our previously reported[32] absorption measurements on ultra-thin HgCdTe
wafers, allowed us to accurately calculate the absorption edge at 20 K and the wavelength re-
sponse of the photodiodes. We were thus able to predict the photodiode cutoff wavelength to
within ±2 μm at 30 μm, which is at least five times more precise than using alloy composition
data.

Figure I-14 shows the relative response as a function of wavelength of three HgCdTe photo-
diodes at 20 K and one device (9B) at 77 K. Eight devices have been measured at 20 K to date,
and seven have shown cutoff wavelengths between 29 and 32 μm. Device 11A in Fig. I-14 has a
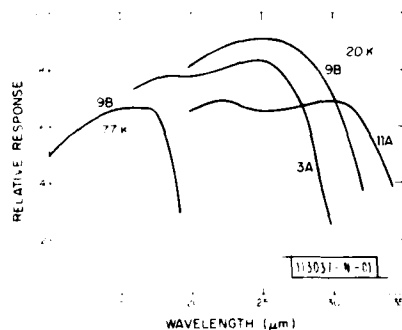
Fig. I-14. Wavelength response of
three high-speed, long-wavelength
HgCdTe photodiodes.

somewhat longer cutoff (34 µm). The quantum efficiency of several of these devices was measured at 77 K with a calibrated, focused CO_2 laser beam and found to be between 50 and 65 percent (65 percent is the theoretical limit of an uncoated HgCdTe photodiode). The responsivity measurements indicate that at 20 K the quantum efficiencies at 25 µm are near 40 percent. This drop in quantum efficiency from that at 10.6 µm is a consequence of the much-longer absorption length ($1/\alpha$ = 9 µm) at 25 µm than at 10.6 µm ($1/\alpha$ = 3.5 µm), and the short minority electron diffusion length (about 10 µm) in the p-type region of these shallow-junction ($w_j \approx$ 3 µm) high-speed photodiodes. In addition, parasitic absorption involving a transition between the light-hole and heavy-hole valence bands is more significant at 25 µm than at 10 µm, which also degrades the internal quantum efficiency. Hole freeze-out at 20 K reduces the carrier concentration in the p-type region to about 1.5×10^{16} cm^{-3} and reduces the parasitic absorption, but it also increases the series resistance of the photodiodes from about 10 Ω at 77 K to about 50 Ω at 20 K.

Fig. I-15. Oscilloscope traces of (a) current pulse into a 20-µm PbSnTe diode laser, (b) response of a $Hg_{0.825}Cd_{0.175}Te$ photodiode to laser pulse, and (c) electrical crosstalk with laser blocked.

2 2-A. 10-ns PULSE
INTO 20-µm DIODE LASER

(a)

RESPONSE OF $Hg_{0.825}Cd_{0.175}Te$
PHOTODIODE TO LASER PULSE

(b)
LASER RADIATION BLOCKED   (c)
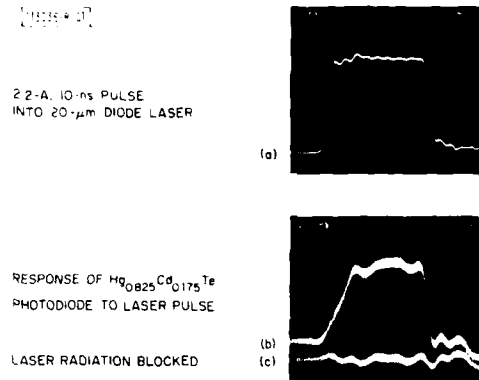
Figure I-15 shows the response of one of these photodiodes at 20 K to a 20-µm PbSnTe diode laser pulse. In the figure, trace (a) is the current pulse into the diode laser, trace (b) is the response of the photodiode to the radiation, and trace (c) is the response of the photodiode with the radiation blocked (showing the electrical crosstalk). The slow rise in the detected signal is due to the turn-on time of the diode laser, as is evident by the fact that the detected laser pulse is 1.5 ns narrower than the current pulse. The very fast fall time (0.6 ns) is indicative of the detector response. Taking into account the 500-MHz bandwidths of both the preamplifier and the oscilloscope, we estimate that the HgCdTe detector also has a bandwidth of about 500 MHz. When the detector bias was reduced from 240 mV in Fig. I-15 to 25 mV, the fall time increased by about a factor of five, indicating RC limited response and a graded carrier concentration of approximately 3×10^{14} cm^{-3}.

The diode laser had a peak output power of about 100 µW; however, only about 7 µW was incident upon the 190-µm-dia. active area of the photodiode as a result of losses in the KRS-5 dewar windows and lenses and an oversized focal spot. The measured peak signal from our photodiode was in agreement with the estimated 50-percent quantum efficiency at 20 µm. Because of this low incident laser power density and high electrical crosstalk, we did not attempt to measure the response of the 90-µm-dia. devices. However, we expect these smaller-area

13

devices to have considerably lower capacitance and therefore to have bandwidths exceeding 1 GHz at 20 μm.

We are in the process of setting up pulse-response measurements at 28 μm. At this wavelength the absorption length is longer (12 to 15 μm), and we anticipate that electron diffusion in the p-type region[33] will degrade the response by 20 to 50 percent. The low shunt resistance of the present devices (30 to 60 Ω) increases the local-oscillator power requirement for shot-noise-limited heterodyne operation at 28 μm to about 150 μW, with an estimated NEP of about 5×10^{-20} W/Hz. With improved surface passivation, the shunt resistance should increase considerably and the LO power requirement should be reduced to below 50 μW.

<div align="right">D. L. Spears</div>

REFERENCES

1. M. W. Fleming and A. Mooradian, IEEE J. Quantum Electron. QE-17, 44 (1981), DTIC AD-A108887.

2. I. Kushima and M. Maeda, IEEE J. Quantum Electron. QE-15, 844 (1979).

3. L. Figueroa, K. Y. Lau, H. W. Yen, and A. Yariv, J. Appl. Phys. 51, 3062 (1980).

4. D. W. Auston, D. M. Johnson, P. R. Smith, and J. C. Bean, Appl. Phys. Lett. 37, 371 (1980).

5. P. R. Smith, D. W. Auston, D. M. Johnson, and W. M. Augustyniak, Appl. Phys. Lett. 38, 47 (1981).

6. A. P. DeFonzo, Appl. Phys. Lett. 39, 480 (1981).

7. F. J. Leonberger and P. F. Moulton, Appl. Phys. Lett. 35, 712 (1979), DDC AD-A085785/4.

8. A. G. Foyt, F. J. Leonberger, and R. C. Williamson, IEEE Trans. Electron Devices ED-28, 1214 (1981).

9. _____, Proc. SPIE Vol. 269: Integrated Optics (Society of Photo-Optical Instrumentation Engineers, Bellingham, Washington, 1981), pp. 109-114.

10. K. Y. Lau and A. Yariv, Opt. Commun. 35, 337 (1980).

11. F. J. Leonberger, J. N. Walpole, and J. P. Donnelly, IEEE J. Quantum Electron. QE-17, 830 (1981), DTIC AD-A105372.

12. S. Li, Appl. Phys. Lett. 29, 126 (1976).

13. V. Diadiuk, C. A. Armiento, S. H. Groves, and C. E. Hurwitz, IEEE Electron Device Lett. EDL-1, 177 (1980); Solid State Research Report, Lincoln Laboratory, M.I.T. (1979:4), p. 9, DDC AD-A084271/6.

14. H. C. Casey and E. Buehler, Appl. Phys. Lett. 30, 247 (1977).

15. I. Umebu, A.N.M.M. Choudhury, and P. N. Robson, Appl. Phys. Lett. 36, 302 (1980).

16. J. J. Oakes, I. G. Greenfield, and L. D. Partain, J. Appl. Phys. 48, 2548 (1977).

17. J. N. Walpole, private communication.

18. H. F. Taylor, Proc. IEEE 63, 1524 (1976).

19. H. F. Taylor, M. J. Taylor, and P. W. Bauer, Appl. Phys. Lett. 32, 559 (1972).

20. F. J. Leonberger, Opt. Lett. 5, 312 (1980), DTIC AD-A090304/7.

21. S. Yamada, M. Minakata, and J. Noda, Appl. Phys. Lett. 39, 124 (1981).

22. H. F. Taylor, IEEE J. Quantum Electron. QE-15, 210 (1979).

23. F. J. Leonberger, C. E. Woodward, and D. L. Spears, IEEE Trans. Circuits and Systems CAS-26, 1125 (1979).

24. C. D. H. King and J. D. Jackson, Proc. 6th European Conference on Optical Communications, University of York, U. K., 16-19 September 1980, p. 256.

25. S. Yamada, M. Minakata, and J. Noda, Electron. Lett. 17, 260 (1981).

26. F. J. Leonberger, Proc. SPIE Vol. 269: Integrated Optics (Society of Photo-Optical Instrumentation Engineers, Bellingham, Washington, 1981), pp. 64-68, DTIC AD-A108855.

27. K. H. Konkle, S. E. Bernacki, C. E. Woodward, and J. I. Raffel, 1st Gigabit Logic Conf., Orlando, Florida, 3-4 May 1979.

28. D. L. Spears, Infrared Phys. 17, 5 (1977), DDC AD-A046982/5.

29. J. Nishizawa, K. Suto, M. Kitamura, Y. Takase, and A. Ito, Research Institute of Electrical Communications, Tohoku University, Sendai, Japan, RIEC Technical Report No. 35 (1973).

30. T. N. Casselman, J. Appl. Phys. 52, 848 (1980).

31. E. Finkman and Y. Nemirovsky, J. Appl. Phys. 50, 4356 (1979).

32. Solid State Research Report, Lincoln Laboratory, M.I.T. (1981:1), p. 5, DTIC AD-A103887; also D. L. Spears and P. E. Duffy (unpublished).

33. D. L. Spears, in Proc. Intl. Conf. on Heterodyne Systems and Technology, Part II, Williamsburg, Virginia, 25-27 March 1980, NASA CP-2138, p. 309.

II. QUANTUM ELECTRONICS

A. LASER REMOTE SENSING OF HYDRAZINE, UNSYMMETRICAL DIMETHYLHYDRAZINE, AND MONOMETHYLHYDRAZINE

Laboratory measurements of the differential absorption of hydrazine, unsymmetrical dimethylhydrazine (UDMH), and monomethylhydrazine (MMH) were described in the previous quarterly report.[1] Those measurements have been extended to include the remote sensing of these materials using LIDAR returns from a topographic target located 2.7 km from the laboratory. The measurements presented here constitute the first long-range laser remote sensing of toxic materials, including hydrocarbons.

The measurement technique, including a description of the dual-laser DIAL system and the choice of frequencies used for the differential-absorption measurements of hydrazine, UDMH, and MMH has been discussed previously.[1] For the remote-sensing measurements, a large tank measuring 60 cm dia. × 1.04 m long was placed in the laser beam path between the laboratory and a 1 m × 1 m flame-sprayed aluminum plate which was set at a range of 2.7 km and served as a diffusely reflecting target.

Prior to carrying out the remote-sensing measurements, both the tank and a laboratory absorption cell were filled with nitrogen gas to minimize oxidation effects. Simultaneous measurements were then made of the normalized LIDAR returns and of the laser radiation transmitted through the cell. After establishing the 100-percent transmittance level, a known amount of liquid hydrazine compound was inserted into the cell and average relative transmittance levels were taken after a preset number of pulses from each laser. Shortly after inserting the hydrazine compound into the cell, a larger amount of the same compound was inserted into the nitrogen-filled tank. The results of the simultaneous cell transmittance and LIDAR measurements are given in Figs. II-1 through II-3 for hydrazine, UDMH, and MMH, respectively, and show the differential absorption of the hydrazine compounds as the vapor pressure approaches equilibrium.

The most notable feature of the experimental results, as seen in the figures, is the marked contrast between the smooth variation of the transmitted radiation through the laboratory cell and the relatively large scatter in the LIDAR returns. The deviations from a smooth line in Figs. II-1(a), II-2(a), and II-3(a) of the relative transmittance through the cell were generally less than 1 percent and approached the 0.1-percent digital quantization error of the data acquisition system. By contrast, the average deviation from the smooth lines of the backscattered LIDAR returns [as shown in Figs. II-1(b), II-2(b), and II-3(b)] are of the order of 5 percent, with several points over 10 percent from the smoothed value.

It should be emphasized that the corresponding points for the relative transmittance through the laboratory cell and the LIDAR returns through the tank are based on the same set of laser pulses and identical normalization factors. Therefore, the larger deviations observed from the LIDAR returns must arise from factors occurring outside the confines of the laboratory. These are presumably a combination of laser-beam wander effects and atmospheric instabilities due to turbulence.

These deviations are the major factor limiting the sensitivity of the concentration measurements. As discussed in the previous quarterly report,[1] the minimum detectable concentration of a trace specie n_{min} that can be measured at long ranges is limited by the noise-equivalent

17
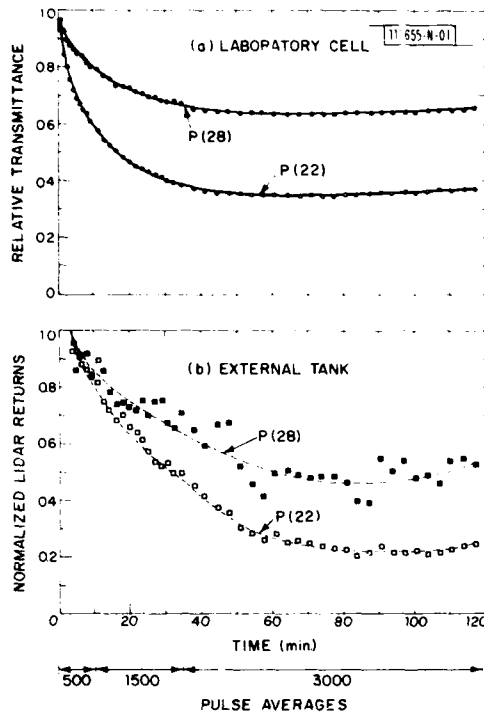
Fig. II-1. Simultaneous differential-absorption measurements of hydrazine in nitrogen-filled laboratory absorption cell and tank. (a) Time variation of relative transmittance through cell after inserting 1.6 μl hydrazine; (b) LIDAR returns from laser pulses passing through tank after inserting 0.8 ml hydrazine. Number of pulses averaged for each point is given below.

Fig. II-2. Simultaneous differential-absorption measurements of UDMH in nitrogen-filled laboratory cell and tank. (a) Time variation of relative transmittance through cell after inserting 5.5 μl UDMH; (b) LIDAR returns from laser pulses passing through tank after inserting 1.95 ml UDMH.

18
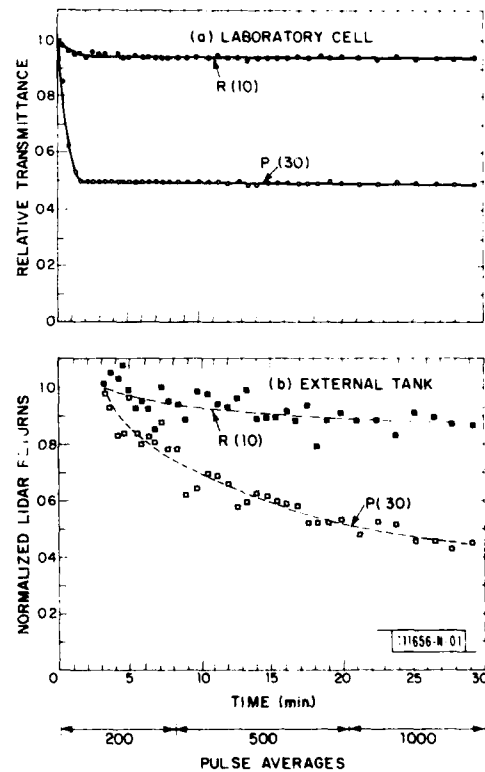
Fig. II-3. Simultaneous differential-absorption measurements of MMH in nitrogen-filled laboratory cell and tank. (a) Time variation of relative transmittance through cell after inserting 6.3 μl MMH; (b) LIDAR returns from laser pulses passing through tank after inserting 1.55 ml MMH.
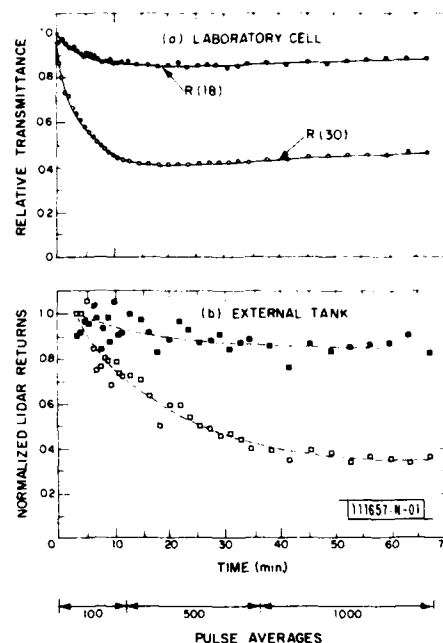
power (NEP) of the detector, and for this particular system is given by

$$n_{min} \text{ (ppb)} = \frac{5.2R}{(\Delta\sigma) \exp[-2\beta R]} \qquad \text{(II-1)}$$

where n_{min} is in units of parts per billion (ppb), $\Delta\sigma$ is the difference in the absorption coefficients of the pollutant at the two wavelengths in units of $(cm\text{-}atm)^{-1}$, R is the range in kilometers, and β is the atmospheric attenuation in km^{-1}. The resulting curve for hydrazine is shown in Fig. II-4 labeled "NEP limited."

Fig. II-4. Minimum detectable average hydrazine concentration by topographic reflection as a function of range.
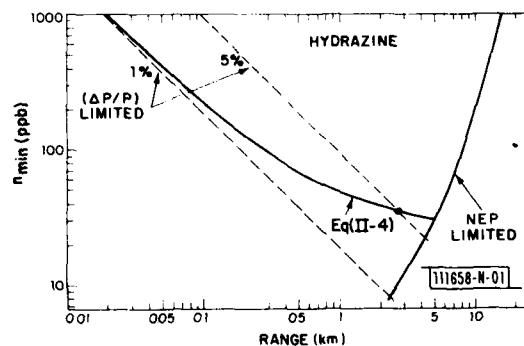
At shorter ranges, a more restrictive limitation can be due to the minimum fractional change in the LIDAR return $(\Delta P/P)$ that can be measured accurately. Normally, $(\Delta P/P)$ is taken as the limit due to equipment limitations (i.e., ≤1 percent) and independent of range, such as is observed in our laboratory cell measurements. Under these conditions, it has been shown[1] that

$$n_{min} \text{ (ppb)} = \frac{5 \times 10^3 (\Delta P/P)}{(\Delta\sigma)R} \qquad . \qquad \text{(II-2)}$$

19

Since the value of $(\Delta P/P)$ must be at least as great as the fractional deviations from smooth behavior to be distinguishable from background fluctuations, a value $(\Delta P/P) = 0.05$ must be used for a range of 2.7 km on the basis of our LIDAR return results. Dashed lines, appropriately labeled for $\Delta P/P = 1$ and 5 percent, are also given in Fig. II-4. However, comparison with the laboratory results ($R \approx 0$) shows the value of $(\Delta P/P)$ required to overcome fluctuations in Eq. II-(2) must itself be considered range dependent. The range-dependent fluctuations are primarily due to laser beam wander and atmospheric turbulence. Although the effect of beam wander on the standard deviation σ_I of LIDAR returns is large, its range dependence is apparently small.[2] Turbulence leads to σ_I values which are strongly range dependent, namely,

$$\sigma_I \approx 0.35 \, C_n k^{7/12} R^{11/12} \tag{II-3}$$

where C_n is the refractive-index structure parameter, and $k = 2\pi/\lambda$ (Ref. 3). It is reasonable to assume that n_{min} involves the sum of contributions due to a range-independent minimum value of $(\Delta P/P)$ and a range-dependent part of $(\Delta P/P)$ which is proportional to σ_I, as given in Eq. II-(3). Then, from Eq. II-(2) one obtains

$$n_{min} = \frac{1}{\Delta\sigma} \left[\frac{5 \times 10^3 (\Delta P/P)_{min}}{R} + C R^{-1/12} \right] \tag{II-4}$$

where $(\Delta P/P)_{min}$ is the minimum value of $(\Delta P/P)$ independent of range, as established by our laboratory measurements, and C is a constant. To obtain n_{min} as a function of range, $(\Delta P/P)_{min}$ was conservatively assumed equal to 0.01, and $C = 80.5$ was obtained by taking the value of n_{min} for $(\Delta P/P) = 0.05$ and $R = 2.7$ km in Eq. II-(2) as a normalization point on the basis of our experimental results. The resulting curve, labeled Eq. (II-4), is shown in Fig. II-4, where it is seen that over intermediate ranges ($0.5 \leqslant R \leqslant 5$ km) the atmospheric effects play the dominant role in limiting the minimum distinguishable pollutant concentration. Curves similar to those in Fig. II-4 have been obtained for UDMH and MMH. The results indicate that average concentrations of 35, 45, and 70 ppb over a range of 2.7 km should be observable for hydrazine, UDMH, and MMH, respectively, and that sensitivities on the order of 100 ppb or better should be achievable between 0.5 and 3 km for all of them.

<div align="right">
N. Menyuk
D. K. Killinger
</div>

B. RAMAN MEASUREMENTS OF STRESS IN SILICON-ON-INSULATOR DEVICES

Device structures fabricated from single-crystal silicon films on insulating substrates are of great interest for a number of applications. Silicon-on-sapphire (SOS) material grown by vapor-phase epitaxy is widely used in the semiconductor industry. A number of alternate growth techniques and material systems are currently under study[4,5] and offer the promise of significant improvements in various physical parameters which affect device performance.

Many of these material systems have a built-in stress on the silicon film due to the different thermal expansions of the substrate and the thin-film silicon between the growth temperature of approximately 1000°C and room temperature. This stress affects device performance since it results in a variation of the silicon energy-level structure and electronic properties. Specifically, for the two-dimensional compressive stress characteristic of SOS, the conduction-band

20

energy-level structure is altered and the heavy-mass directions of the electronic structures are lowered relative to the light-mass directions.[6,7] This results in a higher effective mass and, consequently, a reduced electron mobility. For other materials systems such as silicon-on-fused quartz, the stress is tensile rather than compressive and this results in a higher effective mobiʾity.

Most measurements of this stress have been carried out on large-area wafers of the silicon-on-insulator material. Significant variations in the stress may be expected to occur near the edges of Si structures during the thermal cycling involved in fabricating actual devices from these materials. In particular, the effects of this cycling on the very small structures with linear dimensions less than 1.5 μm currently being fabricated for VLSI applications have not been investigated. Here the use of Raman scattering to probe this stress with a spatial resolution of 1 μm is reported. The variation in the stress across a 6-μm-wide SOS stripe, fabricated as part of a MOSFET, is reported and significant relaxation of the stress at the edges of the device is demonstrated.

Two-dimensional stress results in the splitting of the three-fold degenerate zone-center phonon in Si into a singlet and a doublet. For the ⟨100⟩ face crystals that we have studied, only the singlet is Raman active. The Raman frequency of this mode is shifted in direct proportion to the applied stress.[8,9]

The experiment is shown schematically in Fig. II-5. The 5145-Å argon-ion pump laser beam was reflected from a dichroic mirror and focused onto the sample with a 60X microscope objective. The Raman scattered light was collected by the same objective, transmitted through the dichroic filter, analyzed with a 3/4-m, computer-controlled, double spectrometer, and detected with a small-area, S-20 surface, photomultiplier using photon counting electronics. The computer also controlled a stepping motor which translated the sample in the focal plane of the microscope objective by 0.5-μm increments between spectral scans. A series of spectra corresponding to a line scan across the Si device structure were obtained. These spectra were then analyzed for Raman intensity, frequency shift, and linewidth as a function of position.
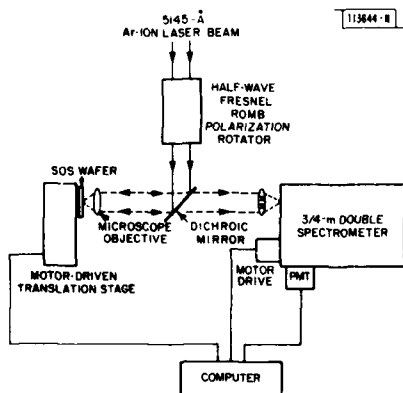

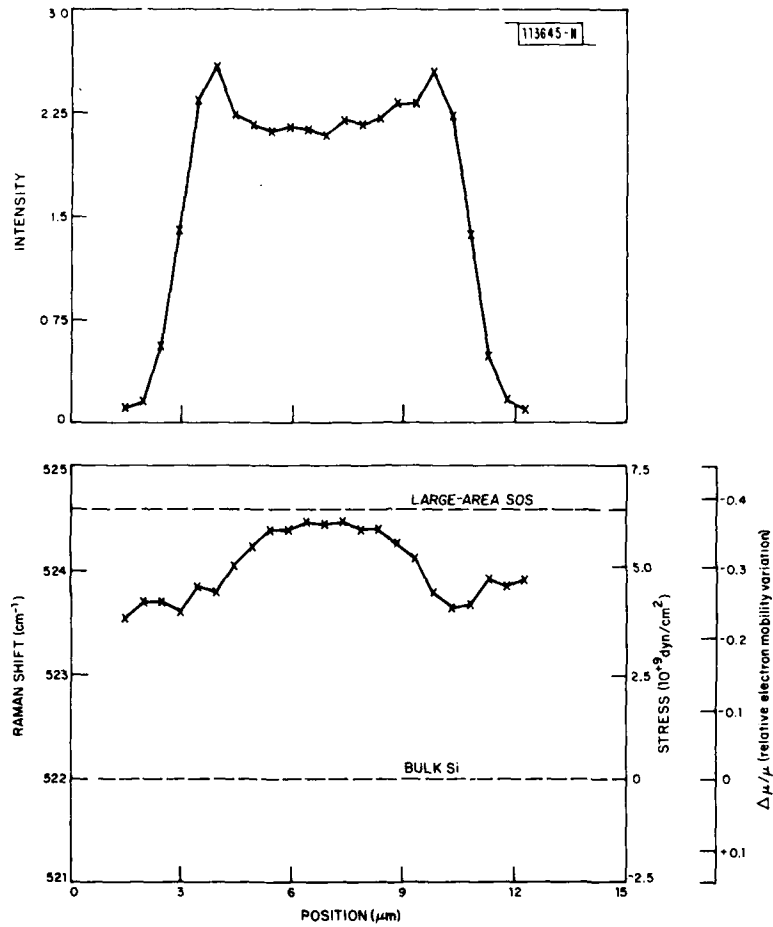Fig. II-5. Experimental setup for measurement of Raman spectra with ~1-μm spatial resolution.

Fig. II-6. Raman intensity and frequency shift measured as a function of position across a 6-μm-wide SOS structure. The stress and electron mobility variations deduced from the measurement are also indicated.

An example of the results of these measurements is shown in Fig. II-6 for a scan across a 6-μm-wide, 0.5-μm-thick SOS structure that was fabricated as part of a MOSFET. The intensity across the structure is shown in the upper curve; the rapid changes in intensity at the edges of the structure indicate that a spatial resolution of ~1 μm has been achieved. The corresponding Raman frequencies are shown in the lower trace. They are shifted to higher frequencies than those corresponding to bulk Si due to the compressive stress of SOS. In the center of the 6-μm structure, only a very small shift from the frequency of large-area SOS (calibration taken from a nearby 50-μm-wide structure on the same wafer) is observed. At the edges of the structure, however, there is a significant shift of the Raman frequency toward the frequency of bulk Si, indicating that a substantial relaxation of the stress has occurred. The stress variation and the corresponding electron mobility variation[6] deduced from these Raman frequency shifts are also shown in Fig. II-6. Similar results have been obtained on silicon-on-quartz structures. These results clearly indicate that the scaling of silicon-on-insulator device structures to micrometer and submicrometer dimensions is accompanied by changes in materials parameters which must be characterized in order to optimize device designs. The utility of Raman scattering as a diagnostic tool to probe these changes with micrometer resolution has been demonstrated. Further experiments on other device structures and silicon-on-insulator materials are under way.

S. R. J. Brueck   D. D. Rathman
T. F. Deutsch   D. J. Silversmith
J. C. C. Fan   B-Y. Tsaur
D. F. Murphy

C. MILLIMETER-WAVE PLANAR-ANTENNA ARRAYS

A planar antenna has been designed which will serve as a subarray element in an imaging array intended for operation over the range 140 to 700 GHz. Scale-model measurements have been carried out at X-band which show that the radiation pattern of the antenna is suitable for such an array.

The subarray element consists of two full-wavelength dipoles separated by a half-wavelength and coupled together by a two-strip transmission line. A Schottky diode is bonded at the midpoint of this transmission line, and the IF signal is brought out at right angles to the dipoles by an extension of the transmission line with appropriate RF filters.

The dipole pair consists of metallic strips evaporated on a quartz substrate. In order that no bulk modes be set up in the substrate, its thickness must be less than the cutoff wavelength in the material. The substrate has a ground plane on its other side which produces an image dipole pair located one-quarter electrical wavelength below the ground plane, thereby sharpening the radiation pattern. Figure II-7(a) shows the details of one subarray element, and Fig. II-7(b) shows the configuration for a 4-element planar array. In the modeling measurements, the antenna pattern was plotted by rotating the element with a computer-driven stepping motor. Typical E- and H-plane radiation patterns are shown in Fig. II-8. The principal lobes have a FWHM of around 80° and are quite smooth and symmetrical, with negligible secondary lobes.

Although the impedance of an isolated full-wavelength dipole is relatively high (~2000 Ω), a number of factors have been incorporated into the present design to lower the measured impedance.

The first millimeter-wave measurements will be carried out at 140 GHz. A mask has been designed by scaling to this frequency, and an antenna array similar to the one shown in Fig. II-7(b)

113646-N

DIPOLES

TRANSMISSION LINE

RF FILTERS

DIODE

CONNECTING
PADS

DIPOLES

(a)

113647-N

(b)
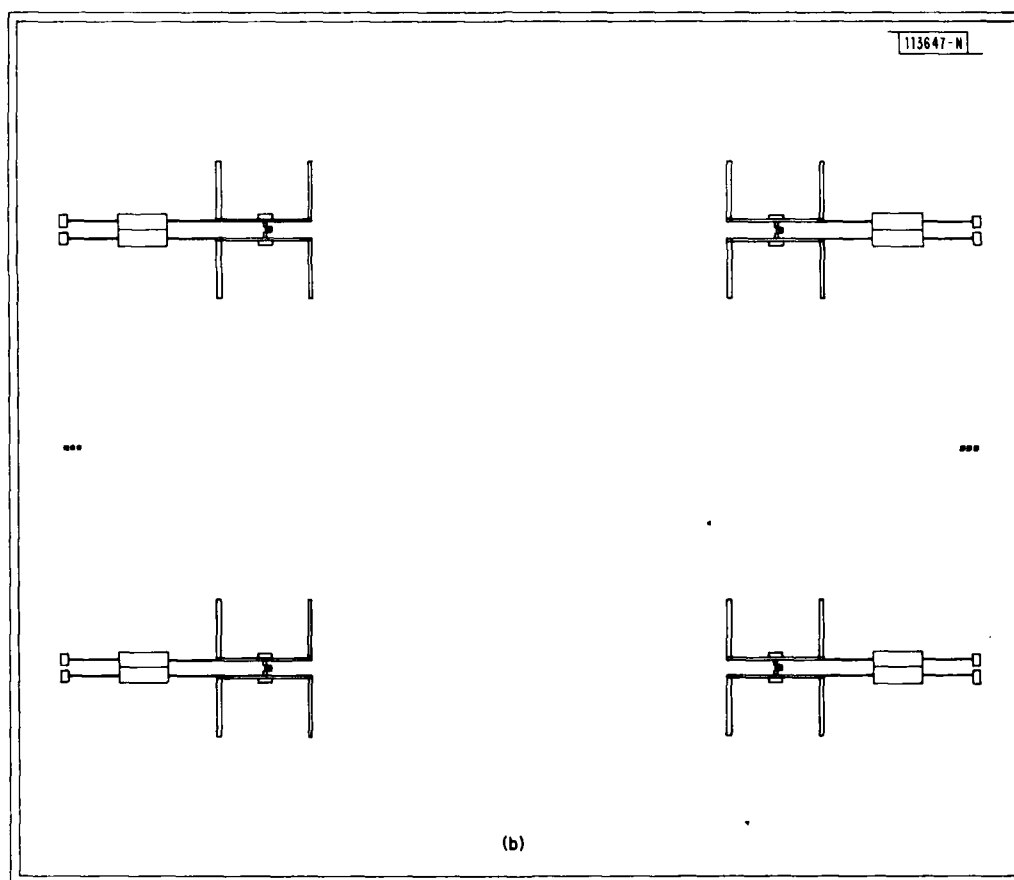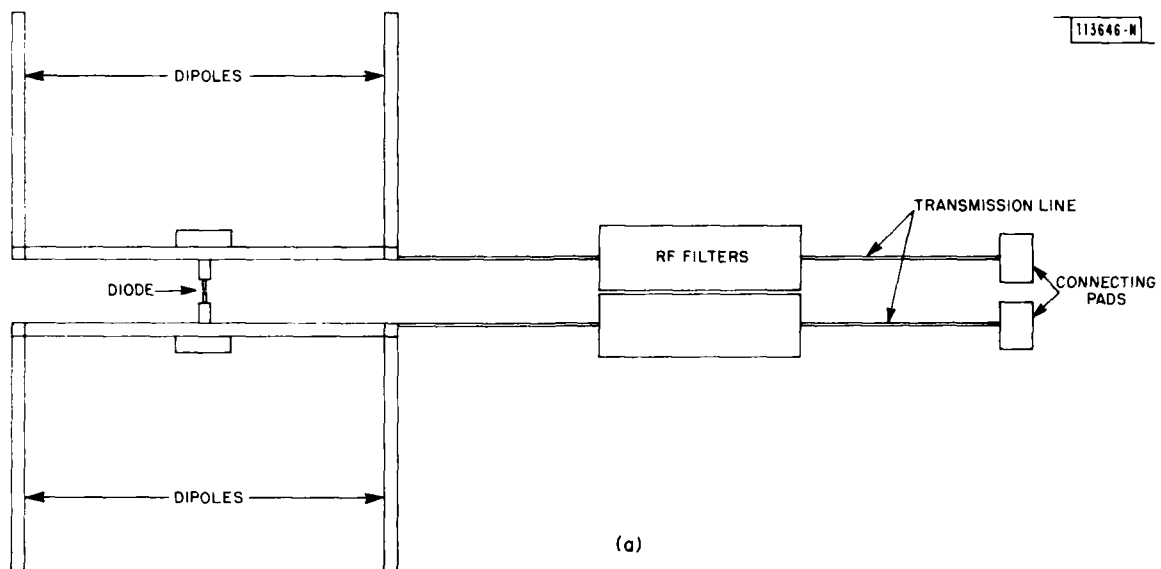
Fig. II-7.   (a) A double-dipole subarray element;   (b) a 4-element array configuration.

24

Fig. II-8.   A typical radiation pattern of one antenna element [Fig. II-7(a)] measured at 9.1 GHz.

E,H FIELD
MAGNITUDE
(linear)

X   E-PLANE
●   H-PLANE
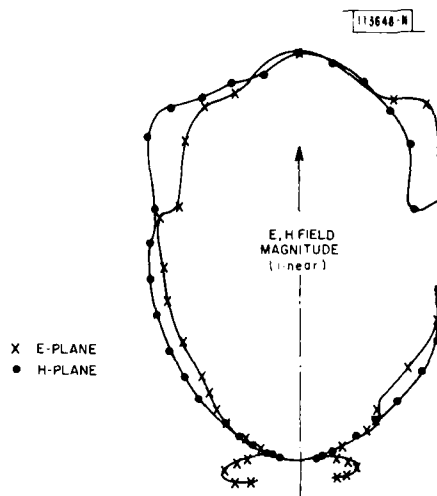
has been made by photolithographic techniques.   Planar GaAs Schottky diodes are being beam-leaded to the center of the dipole configuration, and antenna pattern measurements will be carried out by illuminating the array, which can be rotated in azimuth and elevation for E- and H-plane measurements, with a 140-GHz EIO.   An SIS (superconductor-insulator-superconductor) mixer will be tested in the same double-dipole antenna array; it is currently being fabricated, also for operation at 140 GHz.

Extension of the particular design concept discussed above to 700 GHz is feasible.   All dimensions are well within photolithographic capabilities, and the crucial substrate requirements can be met by using 25-μm single-crystal quartz plates, which have been obtained.

P. Parrish[†]   H. R. Fetterman
G. Sollner[†]   P. E. Tannenwald

REFERENCES

1. Solid State Research Report, Lincoln Laboratory, M.I.T. (1981:3).

2. M. H. Lee and J. F. Holmes, J. Opt. Soc. Am. $\underline{71}$, 559 (1981).

3. R. E. Hufnagel, "Propagation Through Atmospheric Turbulence," Chapter 6 in
    The Infrared Handbook, W. L. Wolfe and G. J. Zissis, Eds. (Office of Naval
    Research, Washington, DC, 1978).

4. J. C. C. Fan, M. W. Geis, and B-Y. Tsaur, Appl. Phys. Lett. $\underline{38}$, 365 (1981),
    DTIC AD-A103036.

5. E. W. Maby, M. W. Geis, Y. L. LeCoz, D. J. Silversmith, R. W. Mountain, and
    D. A. Antoniadis, IEEE Electron Device Lett. $\underline{EDL-2}$, 241 (1981).

6. J. Hynecek, J. Appl. Phys. $\underline{45}$, 2631 (1974).

7. H. Schlotterer, Solid-State Electron. $\underline{11}$, 947 (1968).

8. I. I. Novak, V. V. Baptizmanskii, and L. V. Zhosa, Opt. Spectrosc. (USSR) $\underline{43}$,
    145 (1977).

9. Th. Englert, G. Arbstreiter, and J. Pontcharra, Solid-State Electron. $\underline{23}$,
    31 (1980).

III. MATERIALS RESEARCH

A. STRESS-ENHANCED CARRIER MOBILITY IN ZONE-MELTING-RECRYSTALLIZED POLYCRYSTALLINE Si FILMS ON SiO_2-COATED SUBSTRATES

Preparation of oriented Si films on insulating substrates has been the subject of numerous investigations directed toward the application of Si-on-insulator structures for VLSI/VHSI circuits. We recently described a recrystallization process that uses a movable graphite strip-heater for zone melting polycrystalline Si films deposited on SiO_2-coated Si substrates.[1] The recrystallized Si films, which have (100) texture, consist of large grains with dimensions up to a few millimeters by a few centimeters. N-channel MOSFETs fabricated in these films exhibit surface electron mobilities comparable to those of devices fabricated on single-crystal Si (see Refs. 1 and 2).

This report describes the successful utilization of the movable strip-heater technique for zone-melting recrystallization of polycrystalline Si films deposited on SiO_2-coated fused quartz and sapphire substrates. The crystallographic properties of the recrystallized films are similar to those of the films on Si substrates. (Here and throughout the rest of the report, except in the description of experimental procedure, "substrates" means "SiO_2-coated substrates.") Since the thermal expansion coefficient of Si is 5 to 10 times that of fused quartz, but only 40 to 50 percent that of sapphire, the Si films recrystallized on fused quartz substrates are under a large tensile stress while those on sapphire substrates are under a large compressive stress. Because of the thermal stress, the values of electron mobility in the films on fused quartz and hole mobility in the films on sapphire are higher than the values for the films recrystallized on Si, which are unstressed.

Polycrystalline Si films 0.5 μm thick were deposited by CVD on 0.5-μm-thick SiO_2 layers on ⟨100⟩ Si, fused quartz, or sapphire substrates, as shown schematically in Fig. III-1(a-c). The substrates were 300 to 375 μm thick, with typical lateral dimensions of 2.5 × 2.5 cm. The

109967-N-01
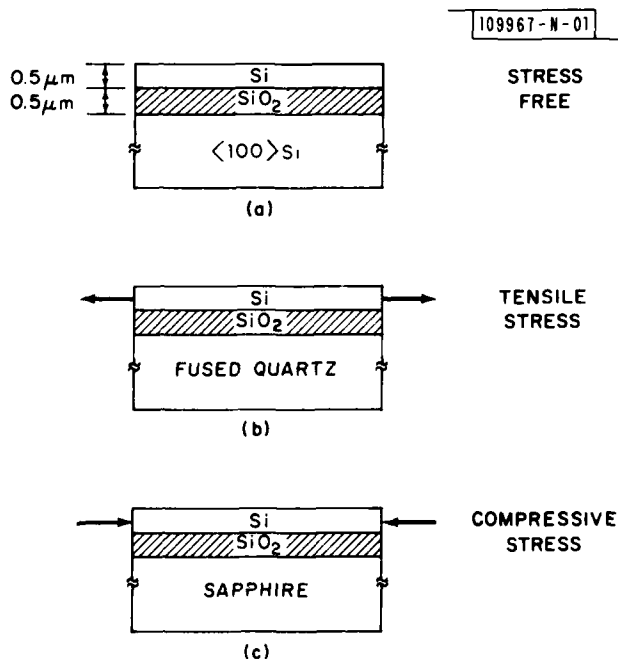
Fig. III-1. Silicon-on-insulator structures incorporating zone-melting-recrystallized Si films. Films on fused quartz and sapphire substrates are under strong tensile and compressive stress, respectively.

27
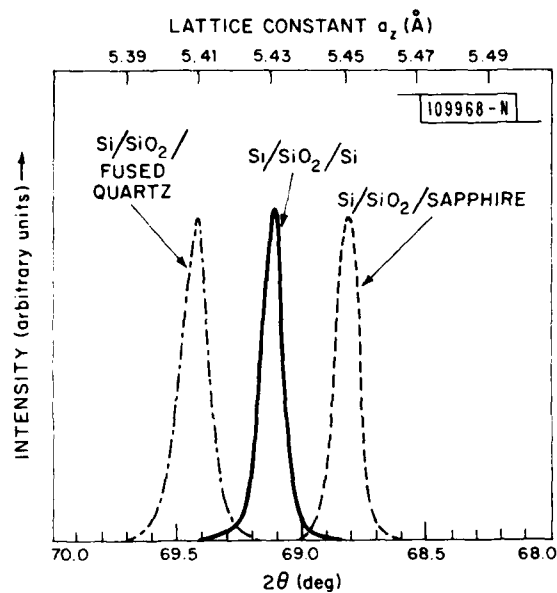
Fig. III-2. X-ray diffractometer traces of (400) peak for Si films recrystallized on three different substrates.

TABLE III-1

PROPERTIES OF RECRYSTALLIZED Si FILMS ON SiO_2-COATED SUBSTRATES

	Electrons				
Substrate	σ_{xy} (kbar)†	N_s (cm^{-2})	μ (cm^2/V-s)	Measured $\Delta\mu/\mu_{Si}$	Calculated $\Delta\mu/\mu_o$
Si	~0.0	4.4×10^{12}	500	—	—
Fused Quartz	+9.6	4.2×10^{12}	870	+0.74	+0.90
Sapphire	−10.2	4.6×10^{12}	325	−0.35	−0.32
	Holes				
Si	~0.0	4.8×10^{12}	180	—	—
Fused Quartz	+9.6	4.0×10^{12}	155	−0.14	−0.05
Sapphire	−10.2	4.2×10^{12}	200	+0.10	+0.06

† "+" for tensile stress, "−" for compressive stress.

28

films were capped sequentially with CVD SiO_2 (~2 μm) and sputtered Si_3N_4 (~300 Å). The composite encapsulating layer greatly enhances the stability of the Si films during the recrystallization process.[1,3] In each recrystallization experiment the sample was placed with the Si film face up on a stationary graphite strip-heater and heated to 1100° to 1300°C. The film was then zone melted by means of a narrow upper strip-heater, which was positioned about 1 mm above the sample surface and scanned across the sample at a speed of 1 to 2 mm/s.

The Si films recrystallized on Si and sapphire substrates are crack-free and have a mirror-smooth surface morphology indistinguishable from that of the as-deposited polycrystalline Si films. The films recrystallized on fused quartz substrates exhibit a slight surface undulation, of the order of a few tens of nanometers. In the initial experiments, in which the cooling rate following zone melting was typically 30° to 50°C/s, these films frequently cracked because of their large tensile stress. Cracking was eliminated by reducing the cooling rate to 5° to 10°C/s.

X-ray diffraction patterns for the recrystallized films contain only the (400) peak, indicating (100) texture. Figure III-2 shows intensity vs angle scans of this peak made with an x-ray diffractometer for three films, one on each type of substrate. For several films of each type, the lattice constant a_z perpendicular to the surface was determined from the angular position of the (400) peak and used to estimate the stress σ_{xy} in the plane parallel to the surface.[4] The average values of stress obtained in this manner are +9.6 kbar for the films on fused quartz and −10.2 kbar for the films on sapphire, where the positive sign denotes tensile stress. The films on Si are nearly free of stress, as expected.

To investigate the effects of stress on the electrical properties of the recrystallized films, Hall and resistivity measurements were used to determine the majority carrier concentration and mobility at room temperature in n- and p-type regions produced by ion implantation followed by thermal activation. The donor and acceptor dopants were 150-keV P-ions and 70-keV B-ions, respectively, implanted to a dose of 5×10^{12} cm^{-2}, and activation was accomplished by furnace annealing at 950°C for 30 min. in N_2 ambient. The implantation-activation process did not cause a detectable change in either surface morphology or in the stress evaluated by x-ray diffraction measurements.

The results of the electrical measurements on the recrystallized films are summarized in Table III-1, which lists the values of sheet carrier concentration N_s and mobility μ. For the films on fused quartz and sapphire substrates, Table III-1 also gives the relative change in mobility $\Delta\mu/\mu_{Si} = (\mu - \mu_{Si})/\mu_{Si}$, where μ_{Si} is the mobility in the films on Si substrates. The values of N_s range from 4.0×10^{12} to 4.8×10^{12} cm^{-2}. For the films on fused quartz, the electron mobility is 74-percent higher and the hole mobility 14-percent lower than the corresponding value of μ_{Si}. This increase in electron mobility is so large that the value for the films on fused quartz, 870 cm^2/V-s, is even higher than the value of ~750 cm^2/V-s measured for bulk single-crystal Si with the same carrier concentration.[5] For the films on sapphire, the changes in mobility are opposite in sign, with the electron mobility 35-percent lower and the hole mobility 10-percent higher than the corresponding value of μ_{Si}.

Since the recrystallized Si films have (100) texture and a high degree of in-plane orientation, their electrical properties can be expected to approximate those of ⟨100⟩ Si single-crystal films that are under isotropic two-dimensional stress. For such a single-crystal film, the relative change in mobility due to a stress σ_{xy} is given by

$$\Delta\mu/\mu_0 \simeq -\frac{(\Pi_{11} + \Pi_{12})\,\sigma_{xy}}{1 + (\Pi_{11} + \Pi_{12})\,\sigma_{xy}} \tag{III-1}$$

where $\Delta\mu$ is the difference between the mobility of the stressed film and the mobility μ_o of the unstressed film, and Π_{11} and Π_{12} are piezoresistance coefficients. We have used Eq. (III-1), together with values of Π_{11} and Π_{12} reported[6] for Si, to calculate the values of $\Delta\mu/\mu_o$ for electrons and holes in single-crystal ⟨100⟩ films subject to the values of stress measured for the films recrystallized on fused quartz and sapphire. The calculated values of $\Delta\mu/\mu_o$, which are listed in the last column of Table III-1, are in satisfactory agreement with the measured values of $\Delta\mu/\mu_{Si}$, in view of the polycrystallinity of the recrystallized films.

The Hall mobility measured for electrons in zone-melting-recrystallized Si films on Si substrates, as listed in Table III-1, is significantly lower than the value for bulk single-crystal Si. However, the electron mobilities determined from the characteristics of n-channel MOSFETs fabricated in such films are comparable to the bulk mobility.[2] This difference can be attributed to a difference in sampling area; the MOSFETs are small enough to lie within a single grain, while the area sampled by Hall measurements is large enough to include a number of grain boundaries. Since there should be a similar difference for the recrystallized films on fused quartz substrates, the electron mobilities for n-channel MOSFETs fabricated in these films should be significantly higher than the bulk mobility, provided that the thermal stress incorporated during recrystallization is retained during device processing. This prediction has been confirmed by initial results that we have obtained for such MOSFETs, which have mobilities as high as 860 cm^2/V-s, compared with 620 cm^2/V-s for single-crystal devices with the same channel doping concentration fabricated in bulk Si.

B-Y. Tsaur
J. C. C. Fan
M. W. Geis

B. CRYSTAL GROWTH OF InP BY THE LEC TECHNIQUE

In an earlier report on the growth of InP by the liquid-encapsulated Czochralski (LEC) technique, we described the development of a growth procedure that gave a high yield of single-crystal (111)-oriented boules because a vertical temperature gradient sufficient to prevent twinning was established at the crystal-melt interface.[7] However, these boules had dislocation densities in the range of 10^4 to 10^5 cm^{-2}. Subsequently, we modified the growth conditions in order to reduce the dislocation density without the use of the technique that has been reported[8] for obtaining dislocation-free InP by heavy doping with Zn, S, or Ge. The first-to-freeze portions of the crystals now being grown are generally either dislocation-free or have very low dislocation densities.

The spatial distribution of dislocations in LEC InP crystals, as revealed by etch-pit patterns on horizontal slices, shows that the dislocations are produced by hoop stresses caused by radial temperature gradients. Shinoyama et al.[9] found that the dislocation density in such crystals can be reduced by increasing the thickness of the B_2O_3 layer used for encapsulating the melt, presumably because this decreases the radial gradients. We therefore modified our earlier procedure by increasing the B_2O_3 thickness from ~1 to ~2 cm. Temperature measurements made by Shinoyama et al.[9] showed that increasing the B_2O_3 thickness also decreases the vertical temperature gradient. To compensate for this effect, as a means of increasing the vertical gradient we increased the flow of heat transported upward through the InP seed by replacing the original BN seed holder with a Ni holder and by soldering the seed directly to the new holder with In. Nevertheless, with the increased B_2O_3 thickness, the initial yield of untwinned crystals was

nearly zero. It was therefore necessary to reduce the minimum vertical gradient required for twin-free growth.

To accomplish the required reduction in the minimum gradient, we have decreased the vibration of the InP seed as it is raised and rotated by modifying the water-cooled pulling rod and its rotation mechanism. A sturdier 1/2-in.-dia. shaft driven by a direct coupling to a motor mounted on the ceiling has replaced the original 5/16-in.-dia. pulling rod. Vertical motion of the new rod is accomplished by a sliding spline in the drive shaft above the high-pressure seal. This seal, which originally consisted of a double O-ring, has been changed to a flat viton gasket. In addition, a Teflon shaft wiper has been substituted for the original aluminum wiper, which abraded the pulling rod. Since making these changes, the yield of twin-free crystals has been quite high even though the vertical gradient has been further reduced by using pure Ar rather than an Ar-He mixture as the high-pressure gas, reducing the gas pressure from 40 to 30 or even 25 atm, and raising the RF coil with respect to the susceptor. We estimate that the vertical gradient is now less than half the gradient that was established under the former conditions.

Etch-pit studies show that the first-to-freeze portions of twin-free crystals grown under the new conditions generally are either dislocation-free or have very low dislocation densities (less than a few times 10^3 cm^{-2}) until their diameter reaches a threshold value of about 20 mm, even when they are nominally undoped. When the diameter increases beyond this threshold, the critical resolved shear stress is exceeded by the hoop stresses, causing a rapid increase in dislocation density. For the larger diameters, the dislocation densities are of the order of 10^4 cm^{-2}. With the goal of increasing the threshold diameter above 20 mm, we are attempting to modify the growth conditions in a manner that will further reduce the radial temperature gradients without increasing the probability of twinning.

To supplement the etch-pit studies, x-ray topography studies have been made on longitudinal sections [generally with (110) surfaces] cut from doped LEC crystals and polished to a thickness of 150 to 300 µm. Transmission projection topographs confirm that the material is nearly dislocation-free up to a diameter of about 20 mm. The most striking feature of the topographs is the large number of prominent growth striations they reveal. Such striations are shown clearly in Fig. III-3, a topograph taken on an S-doped (110) sample with Ag radiation and (111) diffraction vectors. The discontinuities observed in many of the striations are presumably due to remelting,

Fig. III-3. X-ray topograph of longitudinal (110) slice from an S-doped LEC InP crystal.
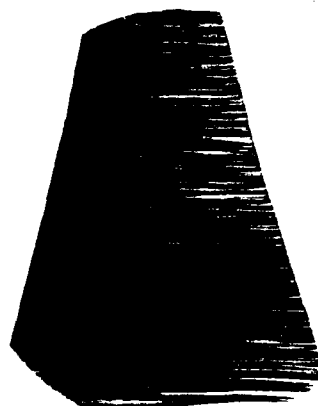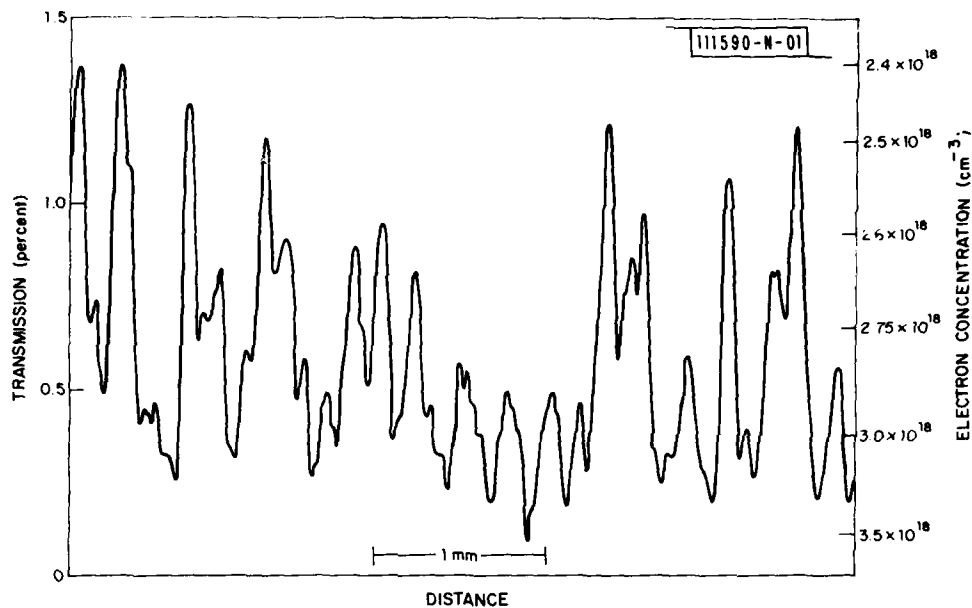
Fig. III-4. Recorder trace showing transmission of CO_2 laser radiation vs distance along vertical direction for S-doped LEC InP crystal.
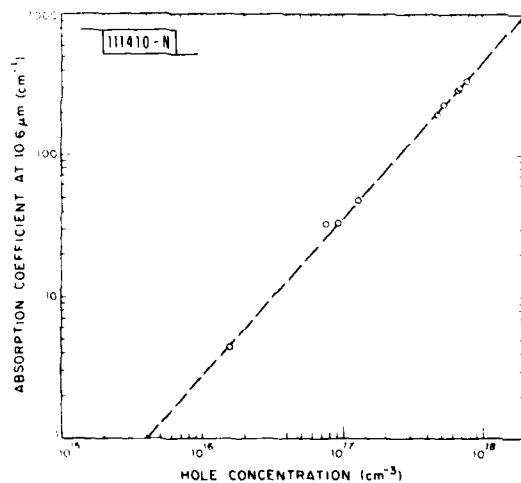

Fig. III-5. Absorption coefficient at 10.6 μm vs free hole concentration for p-type InP samples.

which may be caused by asymmetric radial temperature gradients in the melt. These gradients may evolve because the termination of the RF coil at top and bottom destroys the radial thermal symmetry, although the susceptor rotation should reduce this effect.

We have made free-carrier absorption measurements on LEC crystals doped with S, Sn, or Cd to concentrations of the order of 10^{18} cm^{-3} which show that the growth striations are associated with large variations in dopant concentration. These measurements are performed by determining the variation in infrared transmission as a longitudinal section of a crystal is scanned across the focused beam of a CO_2 laser. Figure III-4 is a recorder trace, obtained by a vertical scan of an x-ray topography sample 160 μm thick, showing the variation in transmission with distance along part of an S-doped, n-type crystal. An electron concentration scale, shown as the right-hand ordinate of Fig. III-4, was constructed by using the data of Walukiewicz et al.[10] for the absorption of CO_2 laser radiation by InP as a function of electron concentration. The apparent concentration in the sample varies from about 2.4×10^{18} cm^{-3} to more than 3.5×10^{18} cm^{-3}. Similar relative variations in carrier concentration are revealed by the transmission measurements on Sn-doped crystals, which are also n-type, and on Cd-doped crystals, which are p-type. Since no data have been published on the free-carrier absorption of p-type InP, in order to evaluate the carrier concentrations in the Cd-doped crystals we have initiated a study to determine the absorption coefficient at 10.6 μm as a function of hole concentration. The data obtained so far are plotted in Fig. III-5 and show that holes have a much larger cross section than electrons. For example, for a carrier concentration of 1×10^{18} cm^{-3} the absorption coefficient at 10.6 μm is about 500 cm^{-1} for p-type material, compared with about 75 cm^{-1} for n-type material.

The sharp, irregular variations in dopant concentration shown by the transmission measurements are probably produced by random convection currents in the melt, which could also contribute to remelting. As a result of such currents, the liquid forming the boundary layer at the growth interface is replaced by liquid from the bulk of the melt. Since, in the absence of convection, the impurity concentration in the boundary-layer liquid is increased by rejection of impurity atoms from the growing crystal, replacement of this liquid would cause a temporary decrease in the impurity concentration in the melt at the interface, and a corresponding decrease in the concentration incorporated into the crystal.

G. W. Iseler   M. S. Taylor
J. V. Pantano   E. J. Delaney

C. LATERAL GROWTH OF SINGLE-CRYSTAL InP OVER DIELECTRIC FILMS BY VAPOR-PHASE EPITAXY

We previously reported initial results on the preparation of single-crystal sheets of InP over dielectric films by means of lateral growth using the PCl_3-InP-H_2 method of vapor-phase epitaxy (VPE).[11] The effectiveness of this procedure increases as the ratio of the lateral-to-vertical growth rates increases. To reduce the vertical growth rate, substrates with low-index orientations are used.[12] With the objective of increasing the lateral growth rate, we have investigated the dependence of this rate on the crystallographic orientation in the plane of the substrate, with particular emphasis on (100) substrates.

To study lateral overgrowth, patterned substrates are prepared by coating InP wafers with a PSG film 0.1 to 0.3 μm thick and then using photolithographic techniques to produce openings in the film. Under suitable growth conditions, deposition initially takes place only on the InP
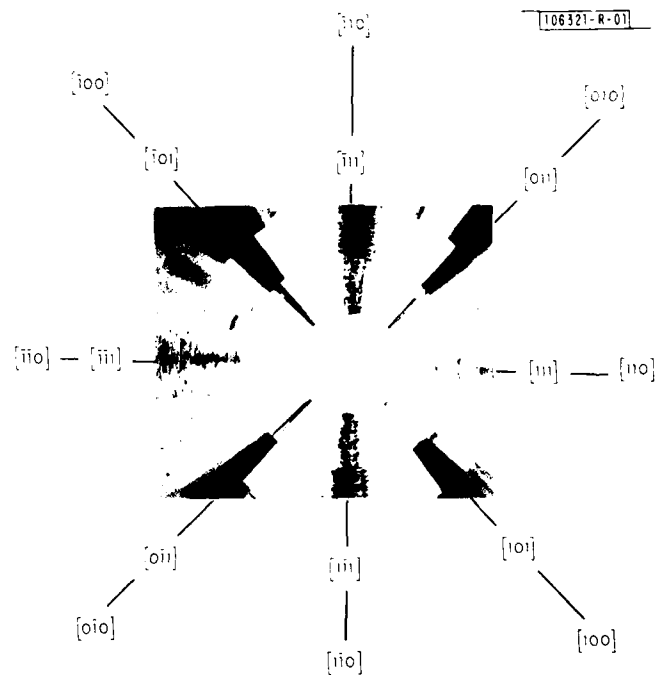
Fig. III-6. Photomicrograph after growth of InP over PSG ring pattern on (100) substrate.
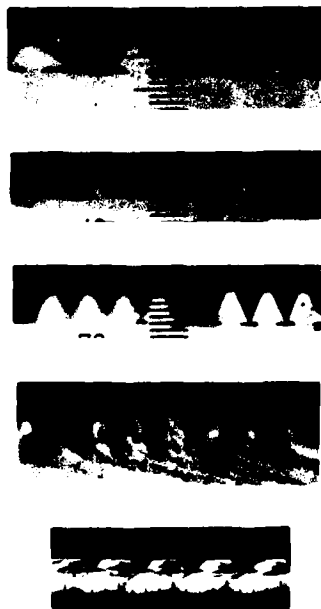

Fig. III-7. Photomicrographs of cleaved cross sections of InP growth over PSG ring pattern on (110) substrate.

34

surface exposed by the openings. When the thickness of the InP epilayer exceeds that of the PSG, this layer can seed lateral growth over the PSG to form a single-crystal overlayer.

For orientation studies we have used a pattern that consists of a central circular opening and a large number of concentric ring openings, each 2.5 μm wide. The PSG not removed consists of several groups of concentric rings. Each such group contains 20 to 30 PSG rings of equal width; this width increases from group to group with increasing distance from the center of the pattern.

Figure III-6 is a photomicrograph taken with vertical illumination after VPE growth of InP over a ring pattern on a (100) substrate. Epitaxial growth nucleated by each ring of exposed InP was followed by lateral growth in radial directions over the adjacent rings of unremoved PSG. In the photomicrograph the brightness varies over a wide range, due to local differences in the character of VPE growth. The central circle is of uniformly high brightness because vertical growth in this region formed a smooth InP epilayer. Outside this circle, dark spokes are observed against a bright background. The bright background occurs in areas where lateral overgrowth formed a smooth InP layer completely covering the rings of PSG, while the dark spokes are located in areas where such a layer was not formed. The most prominent spokes are located along the four [100] and four [110] directions lying in the plane of the substrate.

To investigate the morphology of InP growth in the areas where the PSG stripes were not completely covered by smooth layers, cross sections of samples were prepared by cleaving along {110} cleavage planes perpendicular to the substrate plane. The results are illustrated by Fig. III-7, a photomicrograph showing cross-sectional views obtained at five locations close to a ⟨111⟩ spoke in a growth pattern on a (110) substrate. In all cases, individual growths are bounded by facets formed by slow-growing, low-index planes. Areas in which these growths have triangular or nearly triangular rooftop structures like those shown in the upper four views of Fig. III-7 appear dark when viewed from the top. Such structures, which were obtained along radii lying very close to the low-index directions in the substrate plane, do not yield smooth coverage of the PSG stripes even after extended periods of growth. Structures like those shown in the bottom view, which have a broad flat top parallel to the substrate, will coalesce to form a continuous smooth layer as growth continues. Such structures are formed along radii that deviate sufficiently from the low-index directions.

To use lateral overgrowth of InP for practical applications, we use patterns consisting of parallel stripe openings. In experiments with these stripe patterns, at least one side of the substrate is defined by cleaving along a {110} plane, and the stripes are aligned so that their long axis intersects this side at near-normal incidence. If the stripes were exactly perpendicular to the cleaved side, the directions of lateral growth on (100) substrates would be [110] directions, where smooth lateral growth does not occur.

Figure III-8 shows a cleaved cross section prepared after growth on a (100) substrate patterned with stripe openings making an angle of 10° with the normal to the cleaved side of the

Fig. III-8. Schematic diagram and photomicrograph of cleaved cross section showing growth of InP over PSG stripe on (100) substrate.

1 μm/DIV

35
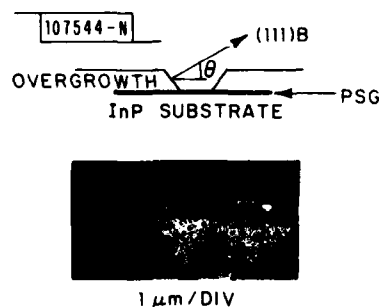
substrate. Lateral growths initiated from two adjacent openings have partially covered the PSG stripe between the openings. Although each growth is bounded at the side by a (111)B facet, growth does not take place on the microscopic scale by a simple combination of growth in two directions — one normal to the substrate and the other normal to the facet. The actual nature of the growth process is indicated by Fig. III-9, which shows a result obtained in another experiment that used a similarly patterned (100) substrate.

Fig. III-9.   Photomicrograph and schematic diagram showing top view of InP growth over PSG stripe on (100) substrate.

Figure III-9 shows a top view of growth along one of the stripes of unremoved PSG. In this region, nucleation on the InP substrate occurred only at a limited number of locations along the two sides of the stripe. Subsequent growth resulted in the formation of InP parallelograms bounded by facets that are labeled f and g in the diagram, where f is a (111)B plane and g is a (110) plane. The relative lengths of facets f and g are such that the parallelograms have one diagonal parallel to the long axis of the PSG stripe. The dark lines bordering the parallelograms in the photomicrograph are observed because both types of facets are inclined with respect to the substrate surface, so that light reflected from the facets is not collected by the microscope. The formation of the (110) facets permits significant lateral growth over the PSG stripe, since the corners between the intersecting (110) and (111)B facets constitute steps that act as nucleation sites for this growth, and new steps are continuously generated as growth proceeds. The rate of lateral growth over the stripe is therefore much higher than it would be if this growth were simply due to the growth normal to the facets that would occur in the absence of the steps [i.e., at the rates of vertical growth measured for (110) and (111)B substrates].

The type of growth shown in Fig. III-9 is too nonuniform for practical applications. With adequate substrate nucleation, successful lateral growth can be obtained for the same geometry. An example of improved growth is shown in Fig. III-10. In this case there was sufficient nucleation for the formation of continuous InP layers that first covered the substrate and then began to grow over the stripe. The (110) and (111)B facets bounding the overgrowths are still apparent,
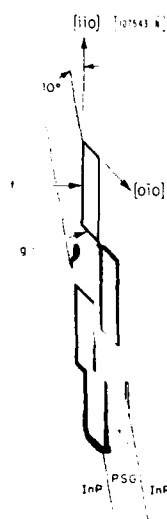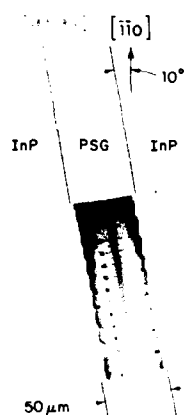
Fig. III-10. Photomicrograph and schematic diagram showing top view of faceted InP growth over PSG stripe on (100) substrate.
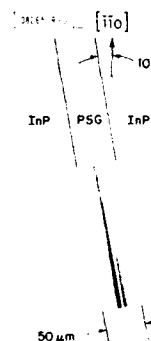
Fig. III-11. Photomicrograph and schematic diagram showing top view of extensive InP growth over PSG stripe on (100) substrate.

but they are much less prominent. Still better lateral growth, of the quality needed for device applications, is illustrated by Fig. III-11 which shows a PSG stripe that has been almost completely covered by featureless InP overgrowths. In this case, discrete (110) and (111)B facets are not observed at the magnification used, although it can be assumed that they are present on a finer scale.

The presence of limiting (110) and (111)B facets, at least on a very fine scale, is characteristic of lateral growth on (100) substrates for a range of stripe directions beginning close to the [110] direction and extending toward the [010] direction. If the angle between the stripe direction and the [110] direction is called θ, this range extends well beyond $\theta = 10°$. At $\theta = 0$, the (111)B facets run parallel to the stripe, no (110) facets are formed, and lateral growth is therefore negligible. Once (110) facets are formed, the lateral growth rate initially increases with increasing θ. If the range in which growth is limited by (110) and (111)B facets extended all the way to the [010] direction, as θ increases the growth rate would increase monotonically to a maximum and then decrease monotonically to a low value when the stripe direction is parallel to the [010] direction, so that only (110) facets are formed. The results in Fig. III-6 show that the actual variation of lateral growth rate with angle is not so simple, implying that facets formed by other crystallographic planes limit the lateral growth over some portion of the angular range.

In utilizing lateral overgrowth to prepare InP/dielectric structures for practical applications, the ratio of lateral-to-vertical growth rates is a critical parameter, since this ratio determines the minimum thickness required to obtain a continuous InP layer for a given separation between stripe openings. The ratio is determined not only by the substrate orientation and the direction of the stripe openings, but also by the growth parameters. Substrate temperature is particularly important, because of its effect on the relative rates of vertical growth on the low-index planes.[12] For growth on (100) substrates using a source temperature of 700°C, we have found that the highest ratios are obtained at substrate temperatures in the vicinity of 650°C. Figure III-12 shows

107545-R-01 ENDS OF STRIPE
OPENINGS

InP
OVERGROWTH

PSG

[110]

Fig. III-12. Photomicrograph showing
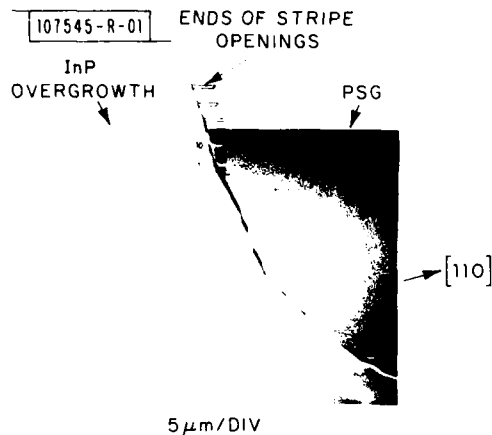top view of continuous single-crystal
InP sheet formed by lateral growth
over PSG film on (100) substrate.

5 μm/DIV

the surface of a continuous single-crystal InP sheet formed by lateral growth in this tempera-
ture range on a (100) substrate with PSG stripes 50 μm wide and stripe openings 5 μm wide.

P. Vohl   A. Chu
C. O. Bozler   A. J. Strauss
R. W. McClelland

D. TRANSIENT ANNEALING OF Se-IMPLANTED GaAs USING A GRAPHITE STRIP-HEATER

We have recently described the utilization of a graphite strip-heater for transient annealing
of ion-implantation damage in Si (see Ref. 13). We now report initial results obtained by using
this technique for annealing GaAs at temperatures up to 1140°C. In earlier experiments on
strip-heater annealing of GaAs, the temperature was limited to 900°C (see Ref. 14).

As a means of achieving very high carrier concentrations, especially with n-type dopants,
ion implantation has been less successful for GaAs than for Si because of difficulties encountered
when GaAs is annealed in order to electrically activate the implanted dopants.[15,16] Although
several encapsulants that are mechanically stable above 1000°C have been reported, conventional
furnace annealing has generally been performed at temperatures of 950°C or below in order to
avoid surface decomposition, excessive diffusion of the implanted species, and changes in sub-
strate carrier concentration. For these temperatures, the peak carrier concentrations obtained
in donor-implanted GaAs are generally limited to the mid-10^{18} cm^{-3} range. Higher electron
concentrations have been achieved by furnace annealing at temperatures up to 1100°C, but this
process has generally produced changes in the substrate carrier concentration. Higher electron
concentrations in the implanted region have also been obtained by transient annealing with laser
and electron beams,[17] but these procedures usually yield low mobilities, which have been attrib-
uted to slip-plane formation caused by thermal stress.[18] These observations indicate the desir-
ability of developing a technique for GaAs annealing that can be used at higher temperatures to
increase the carrier concentration without producing deleterious side effects. The results re-
ported here suggest that the simple, rapid technique of strip-heater annealing has the potential
for meeting these requirements.

Polished semi-insulating GaAs wafers (Cr-doped, $\rho > 10^7$ Ω-cm), oriented 2° off the (100)
toward (110), were implanted at 300°C with a 1×10^{15} cm^{-2} dose of 400-keV Se^+ ions. During
implantation, the wafers were tilted 7° to prevent channeling. Samples cleaved from the im-
planted wafers were encapsulated with a layer of Si_3N_4 about 0.1 μm thick that was plasma-
deposited at 300°C, and with a layer of pyrolytic SiO_2 about 0.4 μm thick deposited at 350°C.

Transient annealing was performed in an Ar-H_2 atmosphere using an experimental setup and procedure similar to those employed in our experiments on Si (see Ref. 13). For an annealing run, an encapsulated sample was placed on a resistively heated graphite strip with the implanted side facing down. The temperature of the graphite strip, as measured with a thermocouple, was raised in about 5 s to a value in the range from 920° to 1140°C, maintained at this maximum value for 10 s, and rapidly lowered to room temperature by turning off the power to the strip. (The maximum temperature was limited to 1140°C because in preliminary experiments it was found that heating to 1150°C caused cracks to form in the encapsulating layers.) The encapsulants were then removed with HF, and the samples were plasma cleaned using DE-100 (oxygenated) gas.

The sheet resistivity ρ_s of annealed samples was measured by the four-point-probe method, and measurements of both ρ_s and the Hall coefficient R_H were made by the van der Pauw method. The values of ρ_s found by the two methods agreed within 5 percent in all cases. Some samples were also characterized by Rutherford backscattering of 2-MeV $^4He^+$ ions to evaluate their crystal quality and by secondary ion mass spectrometry (SIMS) to determine the depth profiles of Se and Si atoms.

Figure III-13 is a semi-logarithmic plot of ρ_s and the sheet electron concentration ($N_s = -1/R_H$) of the ion-implanted, transient-annealed GaAs samples vs the reciprocal of the maximum absolute annealing temperature ($1/T_{max}$). Both sets of data are well represented by straight lines. The activation energy corresponding to the slope of the $\log N_s$ vs $1/T_{max}$ plot is 1.3 eV. As the maximum temperature increases from 900° to 1140°C, ρ_s decreases from about 100 to 25 $\Omega/\square$, N_s increases from 2.7×10^{13} cm^{-2} to 1.8×10^{14} cm^{-2}, and the sheet carrier mobility ($\mu_s = R_H/\rho_s$) decreases from about 2300 to 1400 cm^{2}V^{-1}s^{-1}. Unimplanted control samples from the same GaAs boule all remained semi-insulating after transient annealing, while an ion-implanted sample that was furnace annealed at 950°C for 30 min. had $\rho_s = 35$ $\Omega/\square$, $N_s = 1.1 \times 10^{14}$ cm^{-2}, and $\mu_s = 1600$ cm^{2}V^{-1}s^{-1}.

Fig. III-13. Sheet resistivity ρ_S and sheet electron concentration N_S vs reciprocal of maximum absolute annealing temperature ($1/T_{max}$) for Se-implanted GaAs samples annealed at T_{max} for 10 s.

39
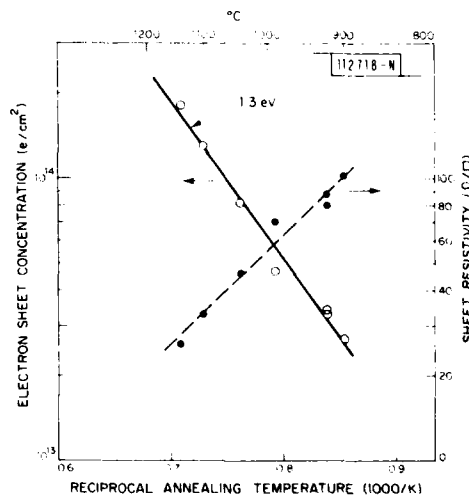
The increase in N_s that we observe with increasing T_{max} can be attributed to an improvement in the crystal quality of the ion-implanted region with annealing, which should increase the concentration of Se atoms occupying lattice sites and decrease the concentration of lattice defects that act as compensating centers. This improvement in crystal quality is demonstrated by the results of the Rutherford backscattering measurements, which were made on samples annealed at 1010° and 1040°C. Figure III-14 shows random and aligned spectra for the sample annealed at 1040°C. The minimum channeling yield (χ_{min}) is 5.5 percent, significantly less than the value of 7.2 percent obtained for the sample annealed at 1010°C. For undamaged GaAs crystals, χ_{min} is about 4 percent.
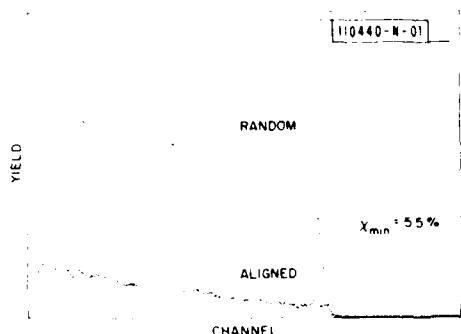

Fig. III-14. Random and aligned spectra for Rutherford backscattering of ^{4}He$^+$ ions from Se-implanted GaAs sample that was annealed at 1040°C for 10 s.
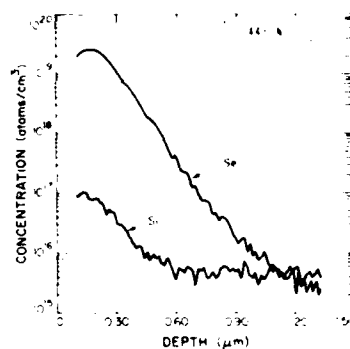
Fig. III-15. Concentrations of Se and Si, as determined by SIMS analysis, vs depth from the surface of a Se-implanted GaAs sample that was annealed at 1100°C for 10 s. Plateau near peak of Se profile is an artifact of secondary ionization mechanism.

Figure III-15 shows the Se depth profile obtained by SIMS analysis of a GaAs sample that was annealed at 1100°C for 10 s. An almost identical profile was obtained for a sample annealed at 920°C. The profiles are in excellent agreement with the profile expected for 400-keV Se$^+$ ions implanted at 300°C; because of enhanced Se diffusion occurring during hot implantation,[19] the expected profile has a deeper tail than the as-implanted profile calculated from simple range statistics. The Se diffusion distances calculated for annealing at 920° and 1100°C for 10 s are only a few tens and a few hundreds of angstroms, respectively, both less than the experimental uncertainty of the SIMS measurements. The peak Se concentration determined by the SIMS analysis is about 3×10^{19} cm^{-3}. Since the solid solubility of Se in GaAs is reported[20] to exceed this value at temperatures of 1050°C and above, the temperature dependence of the solubility should not contribute to the observed dependence of N_s on annealing temperature, at least above 1050°C.

Figure III-15 also shows the Si depth profile for the sample annealed at 1100°C. The total concentration of Si, which is presumably introduced by diffusion from the Si_3N_4 encapsulating layer, is over two-orders-of-magnitude less than the concentration of Se. Therefore, electrons supplied by ionization of Si probably do not make a significant contribution to N_s. The Si concentration is about an order-of-magnitude lower in the sample annealed at 920°C than in the one annealed at 1100°C.

Our results show that good electrical activation of Se-implanted GaAs can be obtained by using a simple graphite strip-heater for transient annealing. From the observed variation of

ρ_s and N_s over the annealing temperature range from 900° to 1140°C, it is probable that still better activation can be achieved by annealing at higher temperatures either with a better encapsulant or in an atmosphere with controlled arsenic vapor pressure.

R. L. Chapman   J. P. Donnelly
J. C. C. Fan   B-Y. Tsaur

E. PRODUCTION AND ANNEALING OF ION-BOMBARDMENT DAMAGE IN SILICIDES OF Pt, Pd, AND Ni

There is great interest in the utilization of metal silicides in Si VLSI technology. As metallization materials, these compounds have the advantage of being much lower in resistivity than polycrystalline Si. Silicide films can be used as self-aligned masks for localized implantation of dopant ions into Si, while dopant implantation through thin silicide contacts has been investigated as a means for fabricating highly doped, shallow-junction devices. In order to insure the reliability of silicide interconnects and contacts exposed to ion bombardment, it is necessary to determine the sensitivity of the silicides to bombardment and also to establish the effectiveness of thermal annealing in removing bombardment damage.

The damage produced by ion bombardment of epitaxial PtSi, Pd_2Si, and $NiSi_2$ films grown on single-crystal Si substrates has been investigated previously.[21] By using ion-channeling techniques it was found that Pd_2Si is relatively insensitive to ion bombardment, while $NiSi_2$ is heavily damaged. In the present work, we have used sheet-resistance measurements to study the production of ion-bombardment damage in polycrystalline films of seven transition-metal silicides (Pt_2Si, PtSi, Pd_2Si, PdSi, Ni_2Si, NiSi, and $NiSi_2$) and the thermal annealing of this damage in three of these compounds (PtSi, Pd_2Si, and $NiSi_2$). The sensitivity of these silicides to ion bombardment is found to increase with increasing heat of formation per metal atom.

The silicide films, except for PdSi, were prepared by electron-beam evaporation of Pt, Pd, or Ni onto ⟨100⟩ Si substrates, followed by heat treatment at 200° to 800°C in a fused-silica tube under flowing forming gas (Ar/H_2). The annealing temperatures and times were selected to produce single-phase silicides. The film of PdSi was formed by using the ion-beam mixing and post-annealing technique reported previously.[22] Backscattering measurements with 2-MeV $^4He^+$ ions indicated that all the silicide films produced were quite uniform, and x-ray diffraction analysis confirmed the expected silicide phase structures.

The films were bombarded with 100-keV Ar^+ ions to doses ranging from 5×10^{14} to 2.5×10^{15} cm^{-2}. During bombardment, the samples were mounted on a copper heat sink whose temperature increased less than 10°C above room temperature. By adjusting the initial metal film thickness, the thickness of each silicide film was selected to be about twice the projected Ar^+-ion range in the film, which is calculated to vary from ~300 Å in Pt_2Si to ~600 Å in $NiSi_2$. The maximum concentration of implanted Ar is estimated to be less than 0.5 at.%. The sheet resistance of each film was measured initially and after successive ion bombardments by using an in-line four-point probe, and the structure was characterized by glancing incidence x-ray diffraction. In the annealing studies, the sheet-resistance measurements were repeated after isothermal annealing of implanted samples for 30 min. at temperatures ranging from 100° to 800°C.

The lattice disorder produced by Ar^+-ion bombardment causes a monotonic increase in the sheet resistance of each silicide film with ion dose. The ratio of the resistance after bombardment to the resistance of the as-prepared film is plotted as a function of dose in Fig. III-16. The
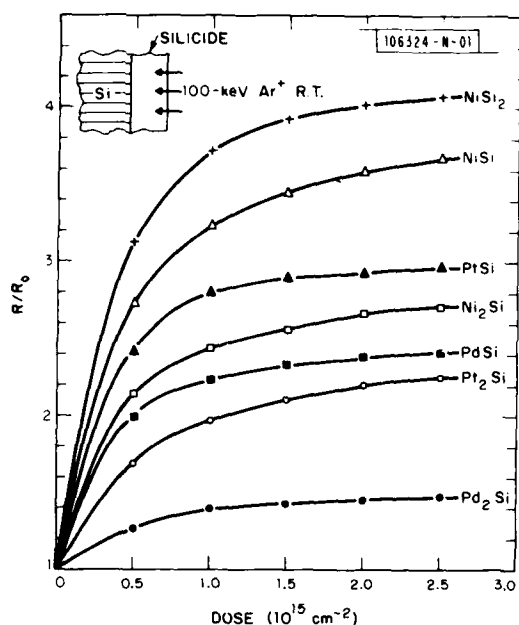
Fig. III-16. Ratio of sheet resistance after ion bombardment R to sheet resistance of as-prepared films R_O as a function of Ar^+-ion dose for Pt, Pd, and Ni silicides.

Fig. III-17. Ratio of sheet resistance after annealing for 30 min. R to sheet resistance of as-prepared films R_O as a function of annealing temperature for films of Pd_2Si, PtSi, and $NiSi_2$ bombarded with 2.5×10^{15} cm^{-2} Ar^+ ions.

TABLE III-2	
HEAT OF FORMATION OF Pt, Pd, AND Ni SILICIDES	
Compound	Heat of Formation per Metal Atom[†] (eV)
Pd_2Si	0.45
Pt_2Si	0.45
PdSi	0.60
Ni_2Si	0.68
PtSi	0.69
NiSi	0.88
$NiSi_2$	0.90
† References 25 and 26.	

42

relative increase in resistance varies systematically among the compounds, with a given dose yielding the smallest relative increase for Pd_2Si and the largest for $NiSi_2$.

Because of the lattice damage produced by ion bombardment, the peaks in the x-ray diffraction spectra of the bombarded films exhibit broadening that increases with ion dose. Although the broadening has not been measured quantitatively, there is a good qualitative correlation between the degree of broadening observed for the different compounds and their relative increase in sheet resistance. Thus the broadening is very small for Pd_2Si, while the diffraction peaks nearly disappear for the most heavily bombarded samples of $NiSi_2$, suggesting the formation of an amorphous phase.

The results of annealing experiments on films of Pd_2Si, PtSi, and $NiSi_2$ bombarded with 2.5×10^{15} cm^{-2} Ar$^+$ ions are shown in Fig. III-17, where the ratio of the sheet resistance after annealing for 30 min. to the resistance of t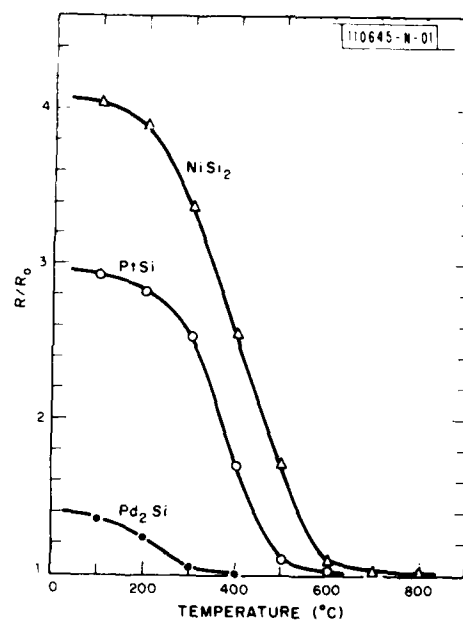he as-prepared film is plotted as a function of annealing temperature. For each compound, there is a threshold temperature above which annealing for 30 min. reduces the sheet resistance to essentially the same value as before ion bombardment. The threshold temperatures for Pd_2Si, PtSi, and $NiSi_2$ are about 300°, 500°, and 600°C, respectively. Comparison with Fig. III-16 shows that the difficulty of removing bombardment damage by annealing increases as the sensitivity to bombardment increases.

An explanation for the observed variation in the sensitivity of the silicides to ion bombardment is suggested by a comparison between the effects of bombardment on crystalline metals and semiconductors. Generally, metals are relatively insensitive to bombardment, while semiconductors are extremely sensitive. This difference in sensitivity is attributed to the difference in chemical bonding between semiconductors and metals, which affects the rate of spontaneous annihilation of bombardment-produced defects such as vacancies.[23] Such annihilation takes place by defect migration, which requires bonds between atoms to be broken and re-formed. Because of the relatively low bond energies that are associated with metallic bonding, the rates of migration and therefore defect annihilation are much higher in metals than in semiconductors, which have higher bond energies due to their characteristic covalent bonding. Consequently, the net damage produced by ion bombardment is much less in metals than in semiconductors.

Since bonding in transition-metal silicides varies over a range that is intermediate between metallic and covalent bonding,[24] we suggest that the observed variation in the sensitivity of the Pt, Pd, and Ni silicides to ion bombardment can be explained mainly by their difference in bonding. Andrews and Phillips[24] have proposed that the degree of covalent bonding in the transition-metal silicides (more precisely, the degree of sp^3 hybridization of the transition-metal atoms) increases with the heat of formation per metal atom $(-\Delta H_f)$. We have therefore investigated whether there is a correlation between $-\Delta H_f$ and sensitivity to ion bombardment for the silicides we have studied. Table III-2 gives the values of $-\Delta H_f$ reported[25,26] for the seven compounds, which are listed in order of increasing sensitivity. It is seen that $-\Delta H_f$ increases monotonically with increasing sensitivity, except that Pd_2Si and Pt_2Si have the same $-\Delta H_f$, although they differ in sensitivity. This excellent correlation between $-\Delta H_f$ and sensitivity supports the hypothesis that the variation in sensitivity is due mainly to differences in bonding.

B-Y. Tsaur
C. H. Anderson, Jr.

REFERENCES

1. M. W. Geis, B-Y. Tsaur, J. C. C. Fan, D. J. Silversmith, R. W. Mountain, J. P. Donnelly, E. W. Maby, and D. A. Antoniadis, 39th Annual Device Research Conference, Santa Barbara, California, 22-24 June 1981.

2. B-Y. Tsaur, M. W. Geis, J. C. C. Fan, D. J. Silversmith, and R. W. Mountain, Appl. Phys. Lett. 39, 909 (1981).

3. E. W. Maby, M. W. Geis, Y. L. LeCoz, D. J. Silversmith, R. W. Mountain, and D. A. Antoniadis, IEEE Electron Device Lett. EDL-2, 241 (1981).

4. B. D. Cullity, Elements of X-Ray Diffraction (Addison-Wesley, Reading, Massachusetts, 1967), Chap. 17.

5. S. M. Sze and J. C. Irvin, Solid-State Electron. 11, 599 (1968).

6. C. S. Smith, Phys. Rev. 94, 42 (1954).

7. G. W. Iseler, J. Cryst. Growth 54, 16 (1981), DTIC AD-A107051; see also Solid State Research Report, Lincoln Laboratory, M.I.T. (1980:3), p. 21, DTIC AD-A094075/9.

8. Y. Seki, H. Watanabe, and J. Matsui, J. Appl. Phys. 49, 822 (1978); G. T. Brown, B. Cockayne, and W. R. MacEwan, J. Cryst. Growth 51, 369 (1981).

9. S. Shinoyama, C. Uemura, A. Yamamoto, and S. Tohno, Jpn. J. Appl. Phys. 19, L331 (1980).

10. W. Walukiewicz, J. Lagowski, L. Jastrzebski, P. Rava, M. Lichtensteiger, C. H. Gatos, and H. C. Gatos, J. Appl. Phys. 51, 2659 (1980).

11. P. Vohl, J. Cryst. Growth 54, 101 (1981), DTIC AD-A107053.

12. Solid State Research Report, Lincoln Laboratory, M.I.T. (1981:3).

13. B-Y. Tsaur, J. P. Donnelly, J. C. C. Fan, and M. W. Geis, Appl. Phys. Lett. 39, 93 (1981); Solid State Research Report, Lincoln Laboratory, M.I.T. (1981:2).

14. B. J. Sealy, R. K. Surridge, S. S. Kular, and K. G. Stephens, in Proceedings of the International Conference on Defects and Radiation Effects in Semiconductors, Nice 1978, J. H. Albany, Ed., Institute of Physics Conference Series No. 46 (Institute of Physics, Bristol, 1979), p. 476.

15. J. P. Donnelly, Nucl. Instr. 182/183, 553 (1981), DTIC AD-A105405.

16. J. S. Williams and H. B. Harrison, in Laser and Electron-Beam Interactions and Materials Processing, J. F. Gibbons, L. D. Hess, and T. W. Sigmon, Eds. (Elsevier North Holland, Amsterdam, 1981), p. 209.

17. See, for example, Laser and Electron Beam Processing of Materials, C. W. White and P. S. Peercy, Eds. (Academic Press, New York, 1980), and Laser and Electron-Beam Solid Interactions and Material Processing, J. F. Gibbons, L. D. Hess, and T. W. Sigmon, Eds. (Elsevier North Holland, Amsterdam, 1981).

18. J. C. C. Fan, R. L. Chapman, J. P. Donnelly, G. W. Turner, and C. O. Bozler, in Laser and Electron-Beam Solid Interactions and Materials Processing, J. F. Gibbons, L. D. Hess, and T. W. Sigmon, Eds. (Elsevier North Holland, Amsterdam, 1981), p. 261.

19. A. Lidow, J. F. Gibbons, V. R. Deline, and C. A. Evans, Jr., Appl. Phys. Lett. 32, 149 (1978).

20. _____ , Appl. Phys. Lett. 32, 572 (1978).

21. H. Ishiwara, K. Hikosaka, and S. Furukawa, Appl. Phys. Lett. 32, 23 (1978).

22. B-Y. Tsaur, S. S. Lau, and J. W. Mayer, Appl. Phys. Lett. 35, 225 (1979).

23. M. W. Thompson, Defects and Radiation Damage in Metals (Cambridge University Press, London, 1969).

24. J. M. Andrews and J. C. Phillips, Phys. Rev. Lett. 35, 56 (1975).

25. C. J. Smithells, Metals Reference Book (Plenum Press, New York, 1967).

26. A. W. Searcy and L. N. Finnie, J. Am. Ceram. Soc. 45, 268 (1962).

A. A NOVEL ANISOTROPIC DRY-ETCHING TECHNIQUE

For many years, reactive ion etching (RIE) has been a primary dry-etching technique. Etching is accomplished by simultaneously impinging a beam of energetic ions and a flux of chemically reactive atoms and molecules on a sample. Both the ions and the reactive flux are produced in the same plasma, which makes independent control of the ions and the reactive flux very difficult. We have developed a technique, called ion-beam-assisted etching (IBAE),[1] which allows independent control of the energetic ions and the chemically reactive flux.

The IBAE system is shown schematically in Fig. IV-1. The gas jet is a 1/8-in. stainless-steel tube located about 1 to 2 mm above the edge of the sample. The tube is capable of supplying reactive gas to the sample at a flux of 5×10^{18} molecules cm^{-2}-s^{-1}. The ion source can direct a beam of positive ions onto the sample with energies from 100 eV to 2 keV and current fluxes up to 1 mA-cm^{-2}. The etching rates obtained with IBAE using a chemically reactive flux of Cl_2 and Ar ions are shown in Table IV-1. The sputter-etching rates for Ar ions are shown for comparison.

Fig. IV-1. Schematic diagram of IBAE system.
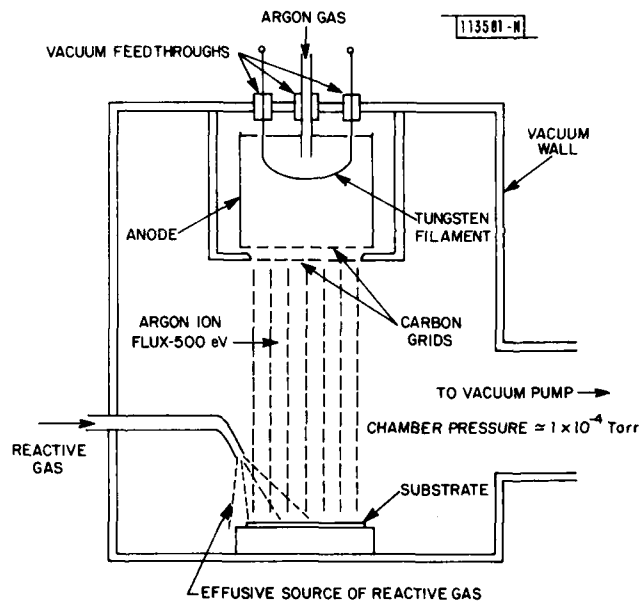
Since the etching rates are dependent upon the reactive flux, a variety of unusual structures can be etched, as shown schematically in Figs. IV-2(a) and IV-3(a). In Fig. IV-2(a), the reactive flux strikes the sample at a shallow angle and the ion beam impinges perpendicularly on the sample surface. As the sample etches, the mask shadows an area on the sample from the reactive gas. In this area, the etching rate is determined primarily by the sputtering rate of the ion beam. Beyond the shadowed area, the sample etches at a rate determined by the combination of the ions and the reactive flux. Figures IV-2(b) and (c) show scanning electron micrographs of GaAs samples which were etched in a manner depicted in Fig. IV-2(a), with the reactive flux impinging from the left. The sloped edge produced from the shadowing of the mask is shown in Fig. IV-2(b). Figure IV-2(c) shows the area where the reactive flux strikes the vertical step in the sample.

TABLE IV-1
NORMALIZED ETCHING RATES OBTAINED WITH IBAE AND WITH ION-BEAM SPUTTERING

Material	Etching Rate (μm-min.$^{-1}$-mA^{-1}-cm^2)	
	IBAE	Sputtering
Al	8.0 to 4.0	0.03 to 0.07
GaAs (n-type)	5.0 to 3.0	0.25
Si	0.4 to 0.3	0.025
SiO$_2$ (thermal)	0.08 to 0.07	0.035
Ni	0.05 to 0.04	0.057
AZ 1350B Photoresist	0.1	0.05

Figure IV-3(a) shows a situation similar to that in Fig. IV-2(a) except that, in this case, the reactive flux reacts with areas of the sample without the assistance of the energetic ions. The reactive flux of Cl$_2$ was made to react spontaneously with the GaAs by heating the sample to about 100°C. The sample is thus being etched by two independent beams, and areas on the sample which are masked from both the reactive flux and the energetic ions remain unetched. Figure IV-3(b) shows a cantilever structure etched into GaAs using the etching technique depicted in Fig. IV-3(a), with the Cl$_2$ flux coming in from the left. Similar structures are shown in Fig. IV-3(c) in which 4- to 5-μm-wide bridges of GaAs span a chasm about 100 μm wide.

It is instructive to note that standard, symmetric, anisotropic etching can be obtained with IBAE by having the reactive flux impinge nearly normal to the sample surface. Figure IV-4 shows a scanning electron micrograph of a 3200-Å-period grating etched about 7500 Å deep into GaAs using IBAE with a normally incident reactive flux. The aspect ratio shown in the scanning electron micrograph is in excess of 10. However, aspect ratios as high as 50 have been obtained using either photoresist or nickel masking materials.

We have thus demonstrated an etching technique which has high etching rates, the ability to etch a variety of structures, and the ability to produce etched surfaces which are of sufficient quality for many GaAs device applications[2] (one of which is discussed in Sec. B below). In addition, this technique allows a greater range of etching conditions to be achieved by virtue of the independent control of the ion beam and the reactive gas.

<div align="right">
M. W. Geis
G. A. Lincoln
W. J. Piacentini
</div>

B. GaAs MESFET WITH GATE RECESS ETCHED BY IBAE

The fabrication of planar MESFETs (Fig. IV-5) requires the formation of ohmic contacts for the drain and source pads, the isolation of devices, and the fabrication of Schottky-barrier gates. The formation of the gate is the most critical operation in the entire sequence, as many device performance parameters are determined at this step. For example, the cutoff frequency of a MESFET is inversely proportional to the gate length, and the saturated drain current, pinch-off voltage, and transconductance are related both to the depletion layer of the Schottky-barrier

NORMALLY INCIDENT
500-eV ARGON IONS

113582-N

OBLIQUELY INCIDENT
REACTIVE GAS FLUX

MASK

RESULTANT PROFILE BY
COMBINED ETCHING OF
DIRECTED ION BEAM AND
REACTIVE GAS

(a)

113584-N

2 μm

2 μm

(b)

(c)
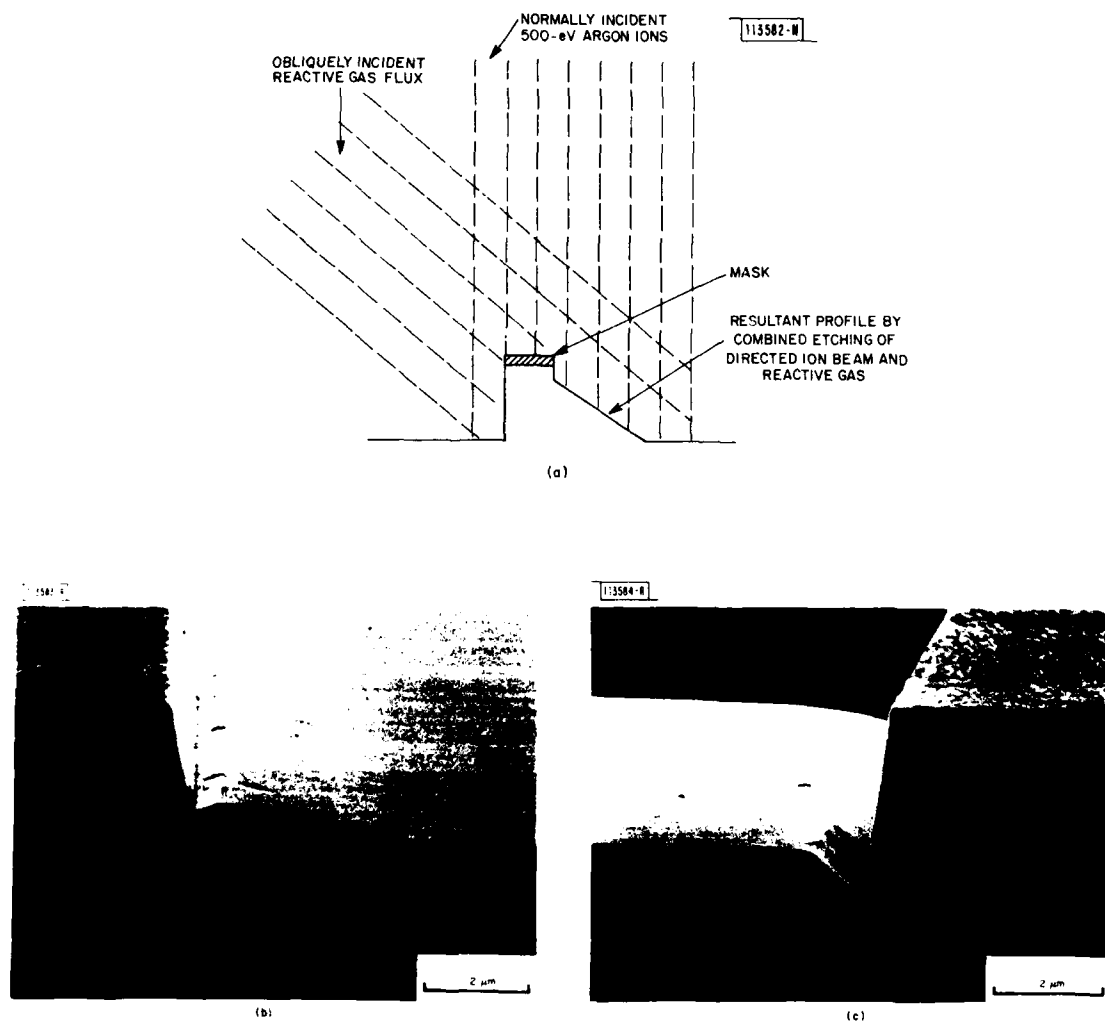
Fig. IV-2. (a) Schematic of a cross-sectional profile obtained by an obliquely incident reactive gas flux and normally incident ion beam. Etching occurs in areas where both reactive flux and ion beam are incident. Areas on sample where only ion beam or reactive flux are incident etch at a much slower rate. (b) and (c) Scanning electron micrographs of GaAs samples which were etched as depicted in (a). Reactive gas impinged on sample from left.

NORMALLY INCIDENT
ARGON IONS

OBLIQUELY INCIDENT
REACTIVE GAS FLUX

113585-S

MASK

RESULTANT PROFILE
BY COMBINED ETCHING
OF DIRECTED BEAM
AND REACTIVE GAS

(a)

(b)

(c)
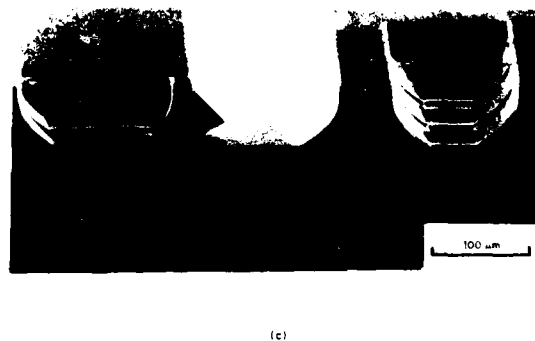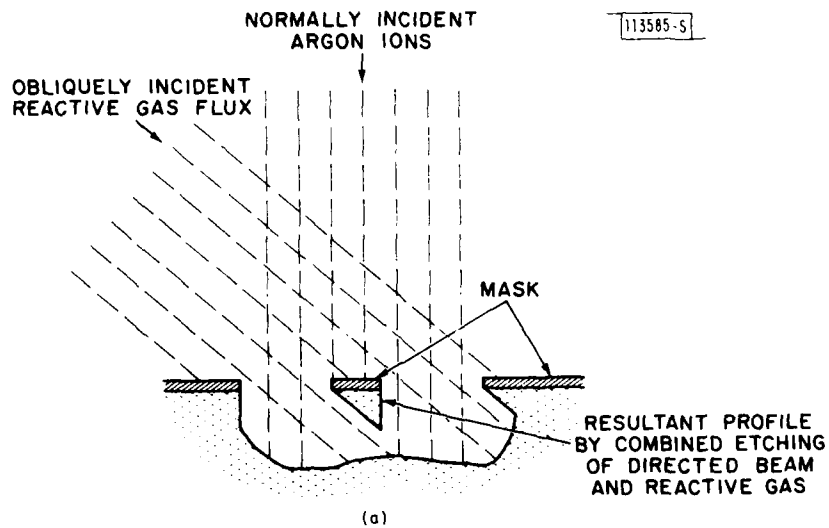
Fig. IV-3. (a) Schematic of a cross-sectional profile obtained by an obliquely incident
ion beam. Etching occurs on sample where either reactive flux or ion beam are inci-
dent. (b) Scanning electron micrograph of GaAs sample which was etched as depicted
in (a). Reactive gas impinged on sample from left. Combined etching of reactive flux
and ion beam resulted in cantilever structure. (c) Scanning electron micrograph of
GaAs sample which was etched as depicted in (a). Combined etching of reactive flux
and ion beam resulted in several bridges about 5 μm wide, spanning a chasm about
100 μm wide.

Fig. IV-4.   Scanning electron micrograph
of an IBAE sample of GaAs.   Reactive flux
and ion beam impinged normally on sample.

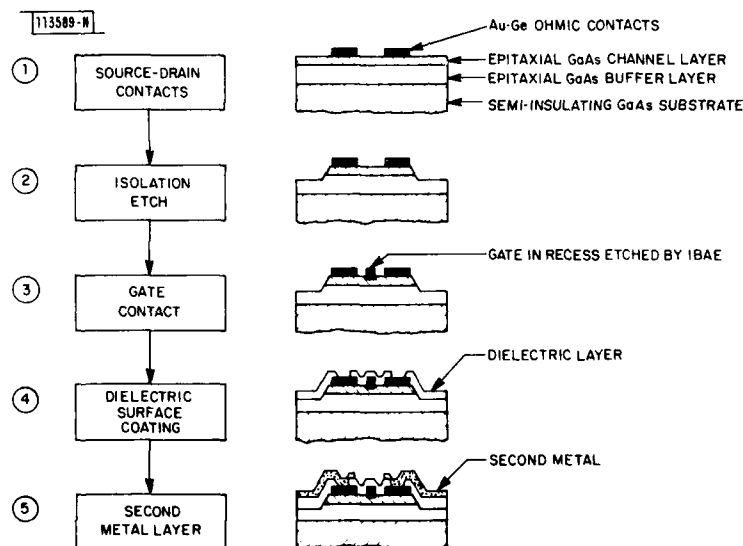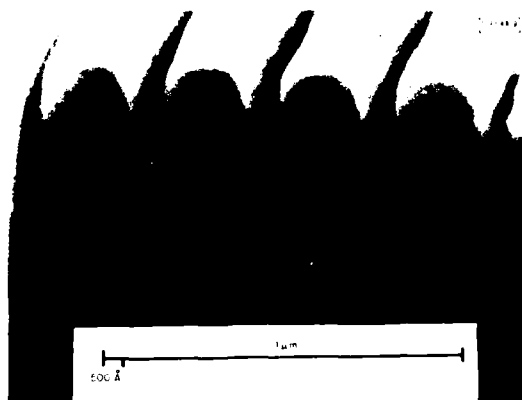Structure consists of 500-Å-wide slots
etched about 0.75 μm deep.

Fig. IV-5.   Fabrication sequence of GaAs ICs based on
IBAE recessed-gate MESFETs.

gate formed in the FET channel and to the quality of the metal-semiconductor contact.   For these
latter reasons, considerable effort has been devoted to the development of techniques for the
treatment of the GaAs in the channel prior to the evaporation of the gate metal.   The recessed
gate is undoubtedly the most important of such developments.

The gate recess improves the reproducibility of Schottky barriers by providing a freshly
etched and oxide-free GaAs surface prior to evaporating the gate metal.   If the gate recess pro-
duces a trough in which the gate fits tightly, the gate depletion layer will be positioned below the
surface depletion of the GaAs material adjacent to the gate, and the drain current will be con-
trolled only by the gate and not influenced by the surface depletion layer adjacent to the gate.
This feature is particularly important for GaAs ICs using a second-level metallization formed
over a dielectric layer (step 5 of Fig. IV-5).   The deposition of the dielectric layer alters the

51

surface states of the GaAs surface near the gate, but the drain characteristics of the device remain unchanged.

An additional benefit of recessing the gate is the reduction of source resistance for a given saturated drain current, due to the thicker conductive layer in the channel on either side of the gate. Furthermore, recessed-gate FETs exhibit small variations of S-parameters with varying power levels,[3] which allows the determination of large-signal characteristics of power FETs from small-signal measurements. It has also been shown[3] that recessed-gate FETs exhibit linear gain at higher power levels and lower third-order intermodulation products. The characteristic dip in the third-order intermodulation product associated with FETs without a gate recess is also eliminated. Since the large-signal operation of FETs at microwave frequencies is related to their switching time,[4] the use of a recessed-gate structure is applicable for digital as well as low-noise and low-power analog applications.

Historically, the gate recess is produced by wet etching the channel prior to gate metallization. However, as FET gate geometries are reduced to submicrometer dimensions, wet etching encounters major limitations. For example, surface tension in small structures produces poor wetting by the solution and nonuniform etching. With submicrometer geometries, the problem of particulate contamination becomes more severe. Wet etching also causes undercutting, and in GaAs the undercutting is proportional to the doping concentration of the etched layer. As a result, wet etching of the gate recess inherently limits the tightness of fit of the gate in the recessed trough. In view of the limitations associated with wet etching, we investigated the use of an alternate novel dry-etching technique, ion-beam-assisted etching (IBAE) of GaAs using Ar ions in a Cl_2 atmosphere, which is discussed in Sec. A above.

The fabrication sequence used to produce a MESFET employing IBAE is shown by the first three steps in Fig. IV-5. After the gate opening is defined on the GaAs in the channel, the wafer is etched for 4.0 min. in a 500-eV, 20-mA-cm^{-2} Ar beam and a Cl_2 atmosphere produced by a flow of 6 cm^3-min.$^{-1}$. Under these conditions, the etched depth is approximately 1700 Å, which is shown in the scanning electron micrograph of the recessed gate in Fig. IV-6. The tight-fitting recess provided for the gate is clearly shown in the micrograph.

Although conventional ion milling and sputtering are also capable of achieving anisotropic etching of GaAs, these techniques produce substantial damage to the etched GaAs. IBAE provides a solution to the damage problem because the chemically reactive species and the ion beam can be independently controlled, thereby providing adequate etch rates while keeping the ion-beam energy below the threshold for damage to the GaAs.

The n-factor of large-area Schottky diodes fabricated on GaAs surfaces etched using IBAE[2] was 1.05, which is adequate for many device applications. We have further investigated the problem of damage when recessing the gate of a MESFET with IBAE by examining the drain characteristics of such a device.

Figure IV-7 shows the drain characteristics of a 250-μm-wide MESFET with a 1.3-μm gate recessed using IBAE. The DC parameters are $ID_{SS} \approx 20$ mA, $g_m = 30$ mS, and $V_p = 1.3$ V. A recess was etched particularly deep in the present device to increase the sensitivity of the drain current to the IBAE. In specific device applications, the required saturation drain currents and pinch-off voltages would vary, higher values being needed for power FETs and zero for enhancement mode devices. The transconductance is, however, a performance parameter invariant with application. The present value of 30 mS compares well with transconductances of devices with conventional gate recesses, which are in the range of 25 to 30 mS

Fig. IV-6. Scanning electron micrograph of evaporated metal gate fitted in gate recess. Etching of gate recess was performed by IBAE.
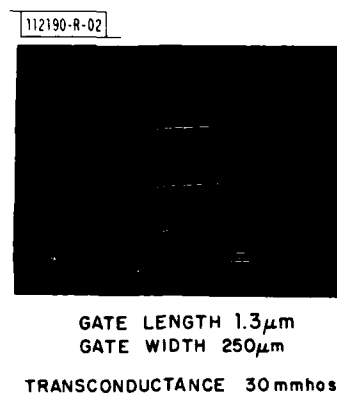

Fig. IV-7. Drain characteristics of GaAs MESFETs with gate recess etched by IBAE.

GATE LENGTH 1.3μm
GATE WIDTH 250μm

TRANSCONDUCTANCE 30 mmhos

(normalized to a gate width of 250 μm), indicating another advantage of IBAE for gate fabrication. The upper trace was included in Fig. IV-7 to show operation of the recessed gate in the enhancement mode with a positive bias of 0.3 V applied to the gate.

Because of the widespread use of GaAs MESFETs for microwave applications, the use of IBAE to produce gate recesses in devices intended for operation at these frequencies will be an important test of this technology. The devices described above have been packaged for microwave operation and will be tested for noise and gain.

In conclusion, FETs with gate recesses etched using IBAE exhibit tight fit of the gate metal in the recess and high values of transconductance. These features are useful to all FETs, but are particularly important to submicrometer gate FETs. The above results indicate the

potentials of IBAE as a powerful processing technology relevant to an important class of microwave devices.

L. J. Mahoney
A. Chu
G. A. Lincoln

REFERENCES

1. M. W. Geis, G. A. Lincoln, N. Efremow, and W. J. Piacentini, J. Vac. Sci. Technol. $\underline{19}$, 1390 (1981).

2. G. A. Lincoln, M. W. Geis, L. J. Mahoney, B. A. Vojak, K. B. Nichols, W. J. Piacentini, N. Efremow, and W. T. Lindley, J. Vac. Sci. Technol. (to be published).

3. T. Sakane, Y. Arai, and H. Komizo, "Large Signal Dynamic Behaviour of X-Band Power GaAs FETs," 1980 Digest of Technical Papers, International Solid State Circuits Conference, San Francisco, California, 13-15 February 1980, pp. 160-161.

4. C. C. Chang, E. Wong, A. Chu, and P. Wang, "The Correlation of the Large Signal Operation of GaAs-MESFETS at Microwave Frequencies with some Selected Low Frequency Electrical Tests," paper presented at the 1978 Workshop on Compound Semiconductor for Microwave Materials and Devices (WOCSEMMAD), San Francisco, California, 13-14 February 1978.

V. ANALOG DEVICE TECHNOLOGY

A. A SAW TAPPED DELAY LINE WITH SHORT (15-ns) PEDESTAL OF DELAY AND HIGH (>100 dB) FEEDTHROUGH ISOLATION

We have previously reported the fabrication of surface-acoustic-wave (SAW) devices with short pedestal of delay and high feedthrough isolation.[1] Design principles and their application to narrow-band test devices have been presented. We report here the incorporation of these design principles into a wide-band tapped delay line for possible use as a multipath simulator for a dense urban environment.

In this device, an edge-bonded transducer (EBT) is used as the input and a surface inter-digital transducer (IDT) is employed as the output, whereby arbitrary filter response may be obtained.

The substrate is YZ LiNbO$_3$ and the center frequency is 175 MHz. The IDT output trans-ducer is 1.6 µs in length with split fingers, and is both apodized and phase modulated by pseu-dorandom phase reversals to produce a noise-like impulse response. Figure V-1 shows an oscillograph of the device impulse response. The top trace is the input impulse (one cycle of 175 MHz) and the bottom trace is the device output. The pedestal of delay is 10 ns. Measure-ment of the direct EM feedthrough shows a suppression greater than 100 dB relative to the input. Feedthrough measurements were made in a system of 250-MHz bandwidth determined by a low-pass filter. Figure V-2 shows the measured device frequency response along with the computed frequency response of the IDT alone. For clarity of presentation, the computed response has been shifted upward an arbitrary amount. It can be seen that the EBT adds some additional roll-off at the edges of the passband; however, the wide-band response of the EBT is evident. Also, except for a shift of 5 MHz in center frequency, the agreement between theory and measurement is quite good. The bandwidth is approximately 100 MHz, although the pseudo-noise character of the output makes the definition of bandwidth difficult.
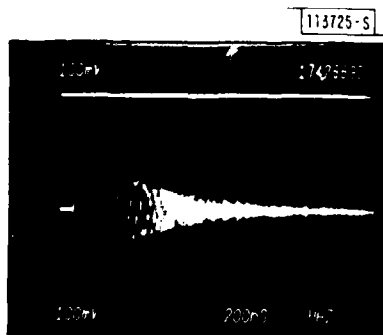

Fig. V-1. Oscillograph of im-pulse response of tapped de-lay line. Top: input impulse; bottom: device output.
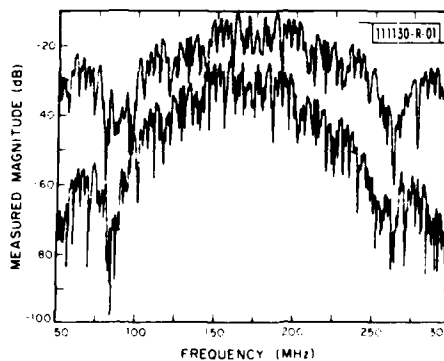
Fig. V-2. Measured (lower trace) and computed (upper trace) frequency re-sponse of wide-band phase-modulated tapped delay line.
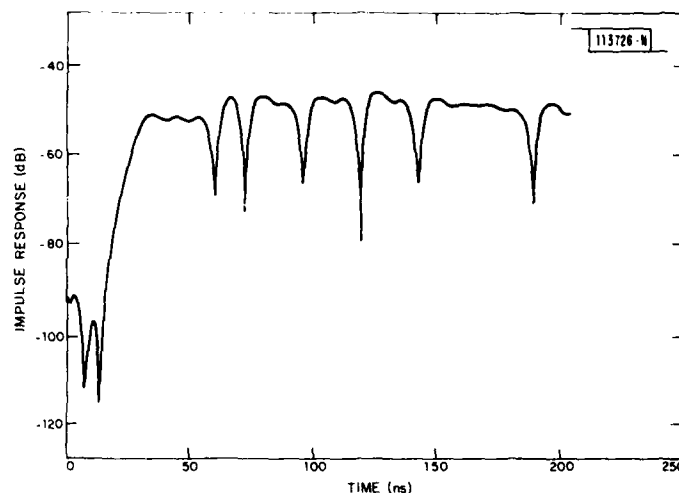
Fig. V-3. Magnitude of impulse response of Fig. V-1. This is Fourier
transform of wide-band network analyzer frequency-response data.

Figure V-3 shows, over the first 200 ns, the magnitude of the impulse response plotted on
a decibel scale. The data are obtained by measuring the CW frequency response (amplitude
and phase) over a 1-GHz bandwidth with an automatic network analyzer; then the Fourier trans-
form of these data yields the impulse response with a time resolution of 1 ns. A 250-MHz
low-pass filter was included at the output of the device. The filter, together with cables. adds
5 ns of delay to the circuit. The delay pedestal of the SAW can be seen to be approximately
10 ns, while the feedthrough is less than 100 dB. The feedthrough should arrive without extra
time delay above that introduced by amplifiers and filters. The first two small peaks shown
in Fig. V-3 are residual feedthrough in both the cables and the network analyzer, and are not
due to the device. In the figure, some of the amplitude weighting can be seen. The deep nulls
in the response result from phase reversals of the taps.

<div style="text-align: right">

D. E. Oates
R. W. Ralston

</div>

B. HIGH-PERFORMANCE ELASTIC CONVOLVER WITH EXTENDED TIME-BANDWIDTH PRODUCT

This report treats the design of an improved elastic convolver which provides, for the first
time, the necessary amplitude, phase, and isolation accuracy that is required in a 2200-time-
bandwidth-product filter. This device has an efficiency of −69 dBm. A number of second-order
effects have been suppressed, most notably the self-convolution, the long-line effect of the out-
put circuit, and the phase dispersion. The emphasis of the discussion is on (1) the dual-track
self-convolution suppression technique, (2) the simplified dual-track output-combining circuit
which minimizes the component count without sacrificing performance, and (3) a transducer
design with built-in compensatory dispersion.

1. Dual-Track Geometry

Self-convolution due to the reflection of SAWs by the opposite transducer is the major output spurious signal existing in the convolver. In order to fully utilize the processing gain provided by the convolver under any circumstances, the self-convolution level should be suppressed by a factor greater than the device time-bandwidth product. The technique we have adopted to solve this problem, as described in an earlier report, is a dual-track-convolver structure[2,3] with a pair of electrically orthogonal transducers as shown in Fig. V-4. With this technique, a self-convolution suppression of greater than 43 dB over the entire passband has been achieved for a 22-μs convolver. This provides the minimum margin of 10 dB in dynamic range needed to support the signal-processing gain.
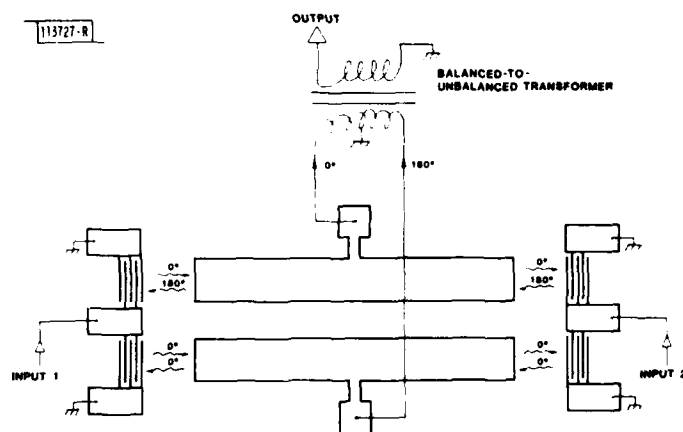

Fig. V-4. Schematic diagram of dual-track convolver structure
for self-convolution suppression.

2. Output Combiner Circuits

Instead of using a balanced-to-unbalanced transformer (balun) to take the difference between the two output plates of the dual-track convolver,[2] as shown in Fig. V-4, the capacitive coupling between the two tracks was exploited to simplify the output circuit. The concept is depicted in Fig. V-5(a-c) which shows the cross-sectional view of the convolver output structure and the local equivalent circuit. The local mixing-product sources of the convolver are represented as ideal voltage sources V_{oc1} and V_{oc2}, C_1 is the mutual capacitance between the two tracks, and C_2 is the capacitance of each individual track to ground. Grounding one output plate and taking the output directly from the other serves the same purpose as the balun. From the equivalent circuit it is apparent that the open-circuit voltage at the output port contributed by the source on track 1 is equal to V_{oc1}, and by the source on track 2 (grounded) is equal to $V_{oc2}\, C_1/(C_1 + C_2)$. Therefore, the capacitance to ground must be made negligible with respect to the capacitive coupling between tracks. This has been achieved by using a thick layer of low-dielectric-constant substrate underneath the LiNbO$_3$, as shown in Fig. V-5(c). A layer of 1/8-in.-thick glass-epoxy circuit board ($\epsilon_r \approx 4.5$) is sandwiched between the 0.028-in.-thick LiNbO$_3$ crystal and package ground.
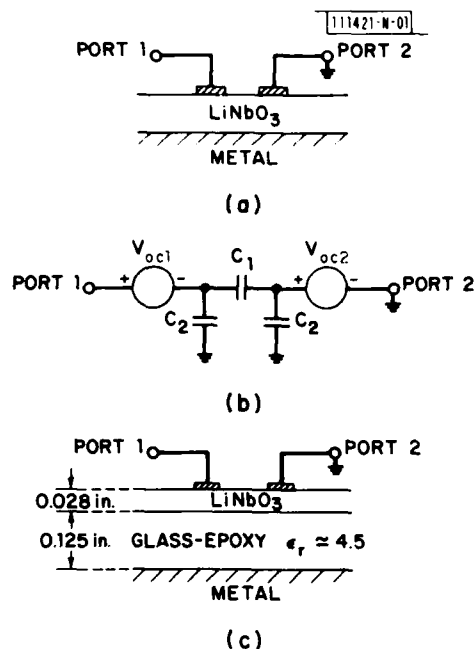
57

Fig. V-5. Dual-track-convolver structure output circuits: (a) cross-sectional view, (b) local equivalent circuit, (c) cross-sectional view of glass-epoxy buffer material to decouple output from package ground.

The second aspect of the output circuit of an elastic convolver with large time-bandwidth product that requires careful design is related to the electromagnetic long-line effect.[4,5] Both amplitude and phase distortions in the time domain result from the slowness of electromagnetic wave propagation within the convolver output plates on high-dielectric-constant materials such as $LiNbO_3$. The design adopted is an equally spaced multiple-tap structure.[2] The long output structure is partitioned into multiple short center-tapped segments. These multiple taps are interconnected through microstrip lines of equal electrical length and impedance to a common point as shown in Fig. V-6(a). The formation of microstrip circuits on low-dielectric circuit board, instead of on the $LiNbO_3$ substrate, serves to reduce the long-line effect. With this technique excellent interaction uniformity of both amplitude ($<\pm0.5$ dB) and phase ($<\pm5°$) are maintained even with very thin output-plate metallization. Thin metallization is required to minimize dispersion due to mass loading. For saving space in the device package, an alternative approach has also been used. The bus-bar approach depicted in Fig. V-6(b) also provides adequate amplitude and phase uniformity. Figure V-7 indicates the amplitude uniformity of convolvers with (a) equal-length and (b) bus-bar outputs.

3. Transducers

Phase dispersion in the frequency domain of an elastic convolver is mainly due to the SAW propagation dispersion. This arises predominately from the mass loading effect of the metal overlay. In order to minimize this effect, the minimum practical metal thickness (50-Å chromium and 300-Å aluminum) is used, and the residual phase distortion is further suppressed by including compensatory phase dispersion in the transducer design.

Simulation indicates, and experiment confirms, that a slightly chirped phase-reversal transducer pair can introduce adequate additional compensatory phase to overcome the residual SAW dispersion within the waveguide. Figure V-8(a-b) shows the measured phase responses of two convolvers in the frequency domain. The use of regular 11-finger phase-reversal transducer pairs resulted in a residual quadratic distortion of 105°. Incorporation of chirped 11-finger phase-reversal transducer pairs provided a reduction of the quadratic distortion to 26°. Thus, the device performance is very close to that of an ideal programmable matched filter.
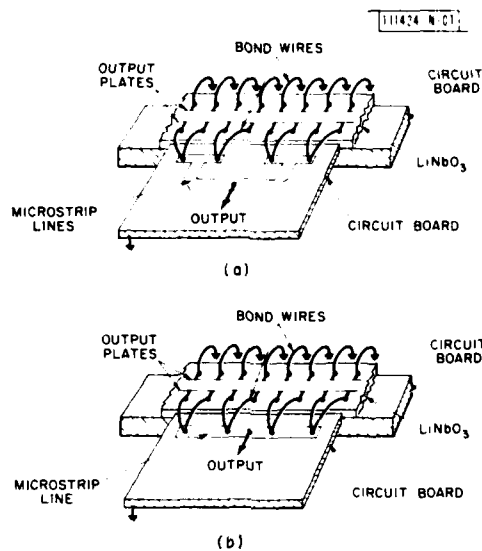
Fig. V-6. Schematic diagrams of convolver output combiner circuits: (a) equal-electrical-length structure, (b) bus-bar structure.

Fig. V-7. Interaction uniformity of elastic convolver: (a) using equal-electrical-length-type output combiner, (b) using bus-bar-type output combiner.
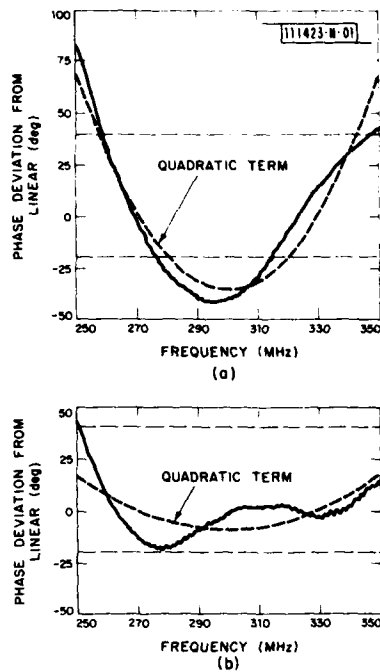
Fig. V-8. Frequency responses of convolver output phase: (a) using 11-finger phase-reversal transducers, (b) using chirped 11-finger phase-reversal transducers.
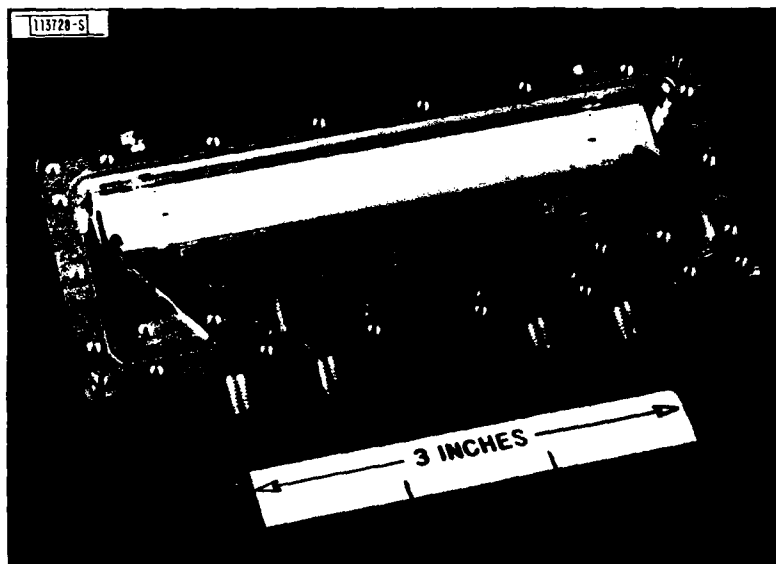

Fig. V-9. Photograph of packaged elastic convolver with time-bandwidth product of 2200.

4. Device Performance

A photograph of the elastic convolver with time-bandwidth product of 2200 is shown in Fig. V-9. It employs a dual-track structure with an orthogonal pair of transducers. These chirped 11-finger phase-reversal transducers have 33-wavelength-wide apertures and feed parabolic horns[2,3] which compress the SAWs to two 3-wavelength-wide waveguides. Each horn is merely 0.5 μs (1.7 mm) in length. The waveguides also serve as output plates. The convolving region is 22-μs long and is broken into two 11-μs segments for demodulating differential-phase-shift-keyed (DPSK) signals. Each segment is tapped by eight equally spaced bond pads. The pads on one track are wire bonded to the package ground via plated-through holes. Pads on the other track are bonded to the microstrip combiner circuits on the circuit board; a 4:1 transformer provides impedance matching.

The convolution efficiency across the frequency band is shown in Fig. V-10. As is common, this efficiency is given as an F-factor, defined as $F = 10 \log(P_{out}/P_1 P_2)$, where P_1 and P_2 are the input powers and P_{out} is the output power. An F-factor of -69 dBm is observed. The self-convolution output is also included in the plot. As described in detail earlier, subtraction of the outputs from the two tracks results in a self-convolution suppression of greater than 43 dB. The device characteristics are summarized in Table V-1. Note that, due to excellent amplitude and phase behavior, the device performance projects to an implementation loss of only 0.15 dB for a 100-Mchip/s minimum-shift-keyed (MSK) waveform.[6]

I. Yao

REFERENCES

1. Solid State Research Report, Lincoln Laboratory, M.I.T. (1981:3).

2. I. Yao, in 1980 Ultrasonics Symposium Proceedings (IEEE, New York, 1980), p.37, DTIC AD-A102978.

3. B. J. Darby, D. Gunton, and M. F. Lewis, in 1980 Ultrasonics Symposium Proceedings (IEEE, New York, 1980), p.53.

4. D. P. Morgan and J. M. Hannah, in 1974 Ultrasonics Symposium Proceedings (IEEE, New York, 1974), p.333.

5. E. L. Adler, in 1980 Ultrasonics Symposium Proceedings (IEEE, New York, 1980), p.82, DTIC AD-A107060.

6. E. L. Adler and J. H. Cafarella, in 1980 Ultrasonics Symposium Proceedings (IEEE, New York, 1980), p.1, DTIC AD-A107057.
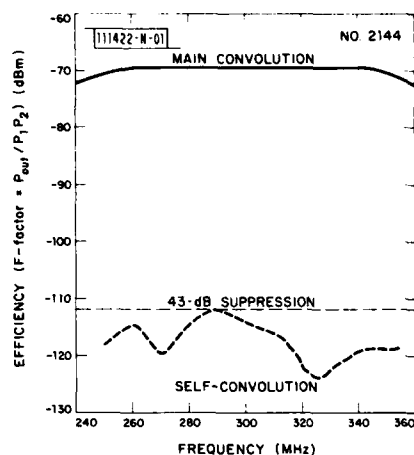
Fig. V-10. Frequency dependence of convolution and self-convolution efficiencies.

TABLE V-1 CHARACTERISTICS OF ELASTIC CONVOLVER		
	Goal	Measured
Time–Bandwidth Product	2200	2200
Time (μs)	22	22
Bandwidth (MHz)	100	100
F–Factor (dBm)	−86	−69
Dynamic Range[†] (dB)	>45	62
Self–Convolution Suppression	>43	>43
Interaction Uniformity		
Amplitude (dB)	±0.5	±0.5
Phase (time domain)	<±10°	±5°
Phase Distortion (frequency domain)	<±30°	<±30°
Implementation Loss[‡] (dB)	<0.25	0.15

[†]Above thermal noise floor with input powers at +20 dBm.

[‡]Calculated for 100-Mchip/s MSK waveform.

SECURITY CLASSIFICATION OF THIS PAGE *(When Data Entered)*

REPORT DOCUMENTATION PAGE		READ INSTRUCTIONS BEFORE COMPLETING FORM
1. REPORT NUMBER ESD-TR-81-332	2. GOVT ACCESSION NO. AD A114189	3. RECIPIENT'S CATALOG NUMBER
4. TITLE *(and Subtitle)* Solid State Research		5. TYPE OF REPORT & PERIOD COVERED Quarterly Technical Summary 1 August – 31 October 1981
		6. PERFORMING ORG. REPORT NUMBER 1981:4
7. AUTHOR(s) Alan L. McWhorter		8. CONTRACT OR GRANT NUMBER(s) F19628-80-C-0002
9. PERFORMING ORGANIZATION NAME AND ADDRESS Lincoln Laboratory, M.I.T. P.O. Box 73 Lexington, MA 02173-0073		10. PROGRAM ELEMENT, PROJECT, TASK AREA & WORK UNIT NUMBERS Program Element No.63250F Project No.649L
11. CONTROLLING OFFICE NAME AND ADDRESS Air Force Systems Command, USAF Andrews AFB Washington, DC 20331		12. REPORT DATE 15 November 1981
		13. NUMBER OF PAGES 80
14. MONITORING AGENCY NAME & ADDRESS *(if different from Controlling Office)* Electronic Systems Division Hanscom AFB, MA 01731		15. SECURITY CLASS. *(of this report)* Unclassified
		15a. DECLASSIFICATION DOWNGRADING SCHEDULE

16. DISTRIBUTION STATEMENT *(of this Report)*

Approved for public release; distribution unlimited.

17. DISTRIBUTION STATEMENT *(of the abstract entered in Block 20, if different from Report)*

18. SUPPLEMENTARY NOTES

None

19. KEY WORDS *(Continue on reverse side if necessary and identify by block number)*

solid state devices	photodiode devices	infrared imaging
quantum electronics	lasers	surface-wave transducers
materials research	laser spectroscopy	charge-coupled devices
microelectronics	imaging arrays	acoustoelectric devices
analog device technology	signal processing	

20. ABSTRACT *(Continue on reverse side if necessary and identify by block number)*

This report covers in detail the solid state research work of the Solid State Division at Lincoln Laboratory for the period 1 August through 31 October 1981. The topics covered are Solid State Device Research, Quantum Electronics, Materials Research, Microelectronics, and Analog Device Technology. Funding is primarily provided by the Air Force, with additional support provided by the Army, DARPA, Navy, NASA, and DOE.

DD FORM 1473 1 JAN 73 EDITION OF 1 NOV 65 IS OBSOLETE

SECURITY CLASSIFICATION OF THIS PAGE *(When Data Entered)*

ATE
MED
8